



---

## Linear and Nonlinear Time-Frequency Analysis for Parameter Estimation of Resident Space Objects

Marco Martorella  
UNIVERSITY DI PISA, DEPARTMENT DI INGEGNERIA

---

02/22/2017  
Final Report

DISTRIBUTION A: Distribution approved for public release.

Air Force Research Laboratory  
AF Office Of Scientific Research (AFOSR)/ IOE  
Arlington, Virginia 22203  
Air Force Materiel Command

<b>REPORT DOCUMENTATION PAGE</b>				Form Approved OMB No. 0704-0188	
<p>The public reporting burden for this collection of information is estimated to average 1 hour per response, including the time for reviewing instructions, searching existing data sources, gathering and maintaining the data needed, and completing and reviewing the collection of information. Send comments regarding this burden estimate or any other aspect of this collection of information, including suggestions for reducing the burden, to Department of Defense, Executive Services, Directorate (0704-0188). Respondents should be aware that notwithstanding any other provision of law, no person shall be subject to any penalty for failing to comply with a collection of information if it does not display a currently valid OMB control number.</p> <p><b>PLEASE DO NOT RETURN YOUR FORM TO THE ABOVE ORGANIZATION.</b></p>					
<b>1. REPORT DATE (DD-MM-YYYY)</b> 21-03-2017		<b>2. REPORT TYPE</b> Final		<b>3. DATES COVERED (From - To)</b> 15 Jun 2014 to 14 Jun 2016	
<b>4. TITLE AND SUBTITLE</b> Linear and Nonlinear Time-Frequency Analysis for Parameter Estimation of Resident Space Objects				<b>5a. CONTRACT NUMBER</b>	
				<b>5b. GRANT NUMBER</b> FA9550-14-1-0183	
				<b>5c. PROGRAM ELEMENT NUMBER</b> 61102F	
<b>6. AUTHOR(S)</b> Marco Martorella				<b>5d. PROJECT NUMBER</b>	
				<b>5e. TASK NUMBER</b>	
				<b>5f. WORK UNIT NUMBER</b>	
<b>7. PERFORMING ORGANIZATION NAME(S) AND ADDRESS(ES)</b> UNIVERSITY DI PISA, DEPARTMENT DI INGEGNERIA VIA GIROLAMO CARUO 000 SNC PISA, 56122 IT				<b>8. PERFORMING ORGANIZATION REPORT NUMBER</b>	
<b>9. SPONSORING/MONITORING AGENCY NAME(S) AND ADDRESS(ES)</b> EOARD Unit 4515 APO AE 09421-4515				<b>10. SPONSOR/MONITOR'S ACRONYM(S)</b> AFRL/AFOSR IOE	
				<b>11. SPONSOR/MONITOR'S REPORT NUMBER(S)</b> AFRL-AFOSR-UK-TR-2017-0023	
<b>12. DISTRIBUTION/AVAILABILITY STATEMENT</b> A DISTRIBUTION UNLIMITED: PB Public Release					
<b>13. SUPPLEMENTARY NOTES</b>					
<b>14. ABSTRACT</b> <p>Since the first space mission in 1957 (Sputnik 1), artificial objects of different size appeared in orbits around the Earth. Nowadays, the number of such objects is estimated to be over 2 millions. More than 300000 of them have a size greater than 10 cm although only 5% of them are catalogued. The observation and tracking of Resident Space Objects (RSOs) has become a crucial task in launch planning of new satellites, collisions-avoidance operations and in general to ensure the safety of operational satellites. The number of space debris has been constantly increasing. Particularly, in 2007 and in 2009, two events (Fengyun antisatellite test and Iridium-Cosmos collision) dramatically increased the number of debris in Low Earth Orbit (LEO). One of the issues related to RSOs tracking and classification regards data and track association, which is the problem of identifying and associating data that is generated by the same object. A possible solution to this problem consists of an extension of the number of parameters (or features) that are used to characterize an object and use them to discriminate it among others. These features can be estimated using both Optical or Radar sensors, which typically perform differently depending on the operational conditions (illumination, distance, etc.). Optical sensors produce a more accurate estimation of the object angular position also with objects that are very distant from the sensor, but are affected by weather conditions (fog, clouds, rain, etc.). Radar sensors, instead, provide accurate range and range-rate measurements and are robust with respect to weather conditions, although they are limited in terms of object distance. The present technical report presents innovative algorithms that exploits coherent radar signals to accurately estimate RSO features to uniquely discriminate an object from others.</p>					
<b>15. SUBJECT TERMS</b> <p>EOARD, space object tracking, space surveillance, space situational awareness, coherent radar systems, nonlinear time-frequency analysis, multi-object tracking, space object characterization</p>					
<b>16. SECURITY CLASSIFICATION OF:</b>			<b>17. LIMITATION OF ABSTRACT</b>  SAR	<b>18. NUMBER OF PAGES</b>  79	<b>19a. NAME OF RESPONSIBLE PERSON</b> MILLER, KENT
<b>a. REPORT</b>  Unclassified	<b>b. ABSTRACT</b>  Unclassified	<b>c. THIS PAGE</b>  Unclassified			<b>19b. TELEPHONE NUMBER (Include area code)</b> 011-44-1895-616022



UNIVERSITA' DI PISA  
DIPARTIMENTO DI INGEGNERIA  
DELL'INFORMAZIONE

## TECHNICAL REPORT

# LINEAR AND NON-LINEAR TIME-FREQUENCY ANALYSIS FOR PARAMETER ESTIMATION OF SPACE OBJECTS

FA9550-14-1-0183

Dipartimento Ingegneria dell'Informazione (DII) - University of Pisa

Authors: L. Gentile, S. Ghio, A. Lupidi, M. Martorella.

LINEAR AND NON-LINEAR TIME-FREQUENCY ANALYSIS  
FOR PARAMETER ESTIMATION OF SPACE OBJECTS

---

## Contents

<b>1</b>	<b>Introduction</b>	<b>4</b>
<b>2</b>	<b>Time Frequency Transforms based RSO features extraction</b>	<b>7</b>
2.1	Time Frequency Transforms . . . . .	7
2.1.1	The STFT . . . . .	7
2.1.2	The WVD . . . . .	8
2.1.3	Cohen's class . . . . .	8
2.2	RSO parameters of interest . . . . .	9
<b>3</b>	<b>Radar Data Simulator</b>	<b>10</b>
3.1	Geometry and signal modelling . . . . .	10
3.1.1	Received signal . . . . .	11
3.2	RSO models . . . . .	14
<b>4</b>	<b>Feature Extraction from radar data</b>	<b>15</b>
4.1	Introduction . . . . .	15
4.2	Features Extraction Algorithm . . . . .	18
4.3	Manual Features Extraction Algorithm . . . . .	18
4.3.1	Functional Block Scheme . . . . .	18
4.3.2	Data Flow . . . . .	19
4.4	Automatic Features Extraction Algorithm . . . . .	21
4.4.1	Functional Block Scheme . . . . .	21
4.4.2	Automatic Point Selection Flow . . . . .	22
4.5	Data Analysis . . . . .	26
4.5.1	Scenario description . . . . .	26
4.5.2	Performance Metrics . . . . .	27
4.5.3	Estimation results . . . . .	28

LINEAR AND NON-LINEAR TIME-FREQUENCY ANALYSIS  
FOR PARAMETER ESTIMATION OF SPACE OBJECTS

---

<b>5</b>	<b>Optical Features</b>	<b>32</b>
5.1	Introduction to photometry . . . . .	32
5.1.1	Definitions . . . . .	32
5.2	Data generation . . . . .	37
5.3	Reference frame and measurement units . . . . .	38
5.4	Data analysis . . . . .	40
5.5	Noise characterization . . . . .	46
5.6	Radar and optical feature summary . . . . .	47
<b>6</b>	<b>Classifiers Description</b>	<b>49</b>
6.1	SVM Classifier . . . . .	49
6.1.1	Binary SVMs . . . . .	49
6.1.2	linear SVM, separable case . . . . .	50
6.1.3	linear SVM, non separable case: Cortes-Vapnik formulation . . . . .	51
6.1.4	Approaches to multi-class classification . . . . .	53
6.2	Bayesian Classifier . . . . .	54
<b>7</b>	<b>Performances Analysis</b>	<b>59</b>
7.1	Optical Only . . . . .	60
7.2	Radar Only . . . . .	65
7.3	Fusion . . . . .	69
<b>8</b>	<b>Conclusions</b>	<b>74</b>
	<b>References</b>	<b>76</b>

## 1 Introduction

Since the first space mission in 1957 (Sputnik 1), artificial objects of different size appeared in orbits around the Earth. Nowadays, the number of such objects is estimated to be over 2 millions. More than 300000 of them have a size greater than 10 cm although only 5% of them are catalogued. The observation and tracking of Resident Space Objects (RSOs) has become a crucial task in launch planning of new satellites, collisions-avoidance operations and in general to ensure the safety of operational satellites. As shown in Fig. 1 the number of space debris has been constantly increasing. Particularly, in 2007 and in 2009, two events (Fengyun anti-satellite test and Iridium-Cosmos collision) dramatically increased the number of debris in Low Earth Orbit (LEO).

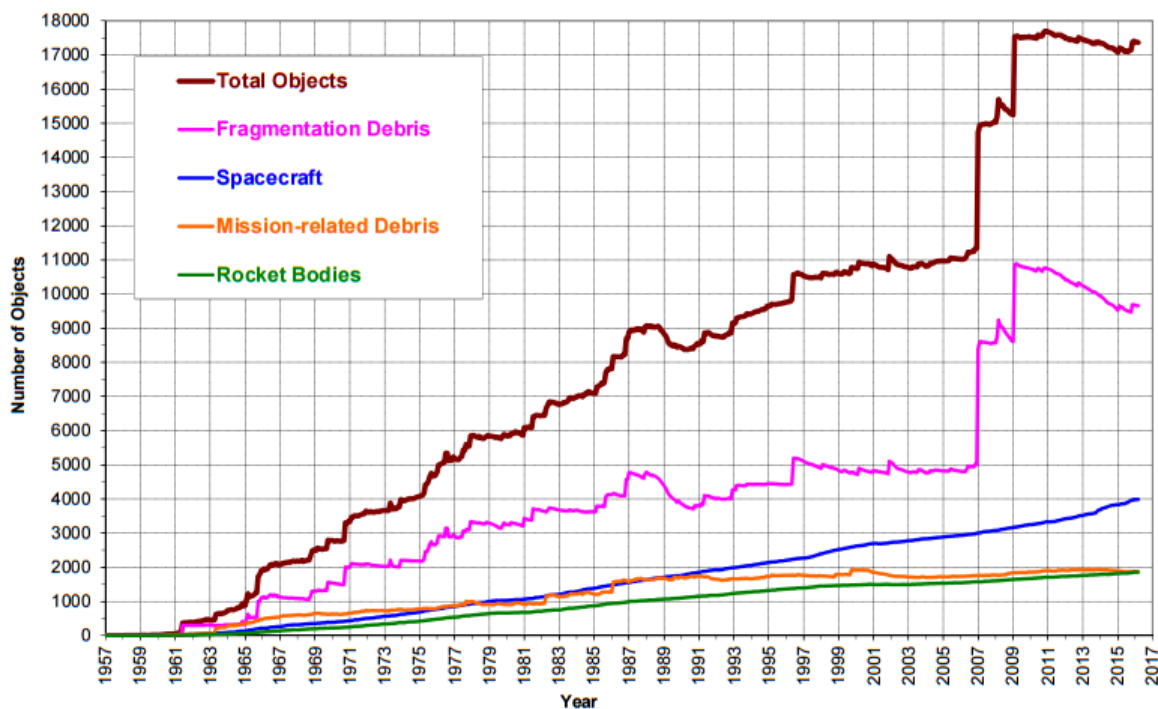


Figure 1: *Distribution of space debris*

Fig. 2 (figure from [1]) also shows that RSOs are more concentrated in low orbits (altitude below 2000 km) and for inclination angles near 90 degrees. As a consequence of these considerations, tracking and prediction of RSO's orbits represent key tasks in Space Surveillance and Tracking (SST) operations.

# LINEAR AND NON-LINEAR TIME-FREQUENCY ANALYSIS

## FOR PARAMETER ESTIMATION OF SPACE OBJECTS

---

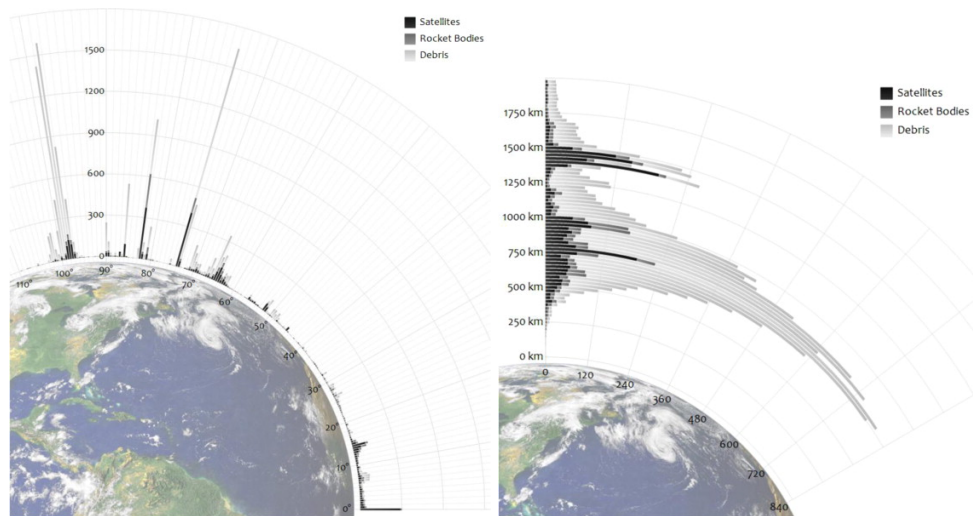


Figure 2: *Distribution of RSO per orbit inclination and per altitude respectively*

One of the issues related to RSOs tracking and classification regards data and track association, which is the problem of identifying and associating data that is generated by the same object. A possible solution to this problem consists of an extension of the number of parameters (or features) that are used to characterize an object and use them to discriminate it among others.

These features can be estimated using both Optical or Radar sensors, which typically perform differently depending on the operational conditions (illumination, distance, etc). Optical sensors produce a more accurate estimation of the object angular position also with objects that are very distant from the sensor, but are affected by weather conditions (fog, clouds, rain, etc). Radar sensors, instead, provide accurate range and range-rate measurements and are robust with respect to weather conditions, although they are limited in terms of object distance. Coherent radar have also the ability to exploit the phase information to estimate object's Doppler signatures and consequently estimate parameters such as their radial velocity, rotation speed, etc. The present technical report presents innovative algorithms that exploits coherent radar signals to accurately estimate RSO features to uniquely discriminate an object from others. Effective radar signal processing based on time-frequency analysis has been proposed to provide the basis for estimators to be developed that ensure both accuracy and robustness against noise. Optical measurement-based algorithms are also reviewed that provide estimates

# LINEAR AND NON-LINEAR TIME-FREQUENCY ANALYSIS

## FOR PARAMETER ESTIMATION OF SPACE OBJECTS

---

of object parameters with the aim of jointly using radar and optical features to improve target discrimination performances with respect to radar-only or optical-only measurements. Results are presented that prove the effectiveness of the algorithm proposed. This technical report is organised as follows:

- In Section 2 Time-Frequency transforms are discussed and parameters of interests are identified.
- In Section 3 the Radar signal model adopted, the signal generation process and different models of RSOs are introduced.
- Section 4 describes the algorithms that have been developed for feature extraction from Radar data. Particularly a manual and an automatic algorithm are presented and discussed.
- In section 5 elements of photometry are reviewed and a model for optical features extraction is presented and applied to the classes identified in Section 3.
- Section 6 concerns the proposed classification algorithms, specifically SVM and Bayesian.
- In Section 7, the algorithm performances are shown and discussed in the case of radar-only measurements, optical-only measurements and after fusing information from both radar and optical measurements.
- Section 8 provides the conclusions and future developments regarding RSOs orbit determination and classification.



## 2 Time Frequency Transforms based RSO features extraction

### 2.1 Time Frequency Transforms

The echo signals generated by rotating objects have spectral contents that change with time (non-stationary signals). Due to lack of localized time information, the widely used Fourier Transform (FT) cannot provide time-varying frequency modulation information. A Joint Time-Frequency Analysis (JTFA) that provides localized time-dependent frequency information is needed for extracting time-varying motion dynamic features. Time-frequency Distributions (TFDs) includes linear and bilinear transforms, such as the Short Time Fourier Transform (STFT) and Wigner-Ville distribution (WVD) respectively.

#### 2.1.1 The STFT

The most standard approach to analyze a signal with time-varying frequency content is to split the time-domain signal into many segments, and then take the Fourier transform of each segment. This is known as the STFT operation and is defined as

$$STFT(t, \omega) = \int s(t')w(t' - t) \exp\{-j\omega t'\} dt' \quad (1)$$

This operation differs from the Fourier transform only by the presence of a window function  $w(t)$ . As the name implies, the STFT is generated by taking the Fourier transform of smaller durations of the original data. Alternatively, we can interpret the STFT as the projection of the function  $s(t')$  onto a set of bases  $w^*(t' - t) \exp j\omega t'$  with parameters  $t$  and  $\omega$ . Since the bases are no longer of infinite extent in time, it is possible to monitor how the signal frequency spectrum varies as a function of time. This is accomplished by the translation of the window as a function of time  $t$ , resulting in a 2D joint time-frequency representation STFT  $(t, \omega)$  of the original time signal. The well-known spectrogram defined as the square modulus of the

STFT is a well-known tool for time-frequency analysis. With a time-limited window function, the resolution of the STFT is determined by the window size. There is a trade-off between the time resolution and the frequency resolution. A larger window has higher frequency resolution but a poorer time resolution and viceversa.

### 2.1.2 The WVD

The WVD of a signal  $s(t)$  is defined as the Fourier transform of the time-dependent autocorrelation function

$$WVD(t, \omega) = \int s\left(t + \frac{t'}{2}\right) s^*\left(t - \frac{t'}{2}\right) \exp\{-j\omega t'\} dt' \quad (2)$$

where  $s(t + t'/2)s^*(t - t'/2)$  can be seen as a time-dependent autocorrelation function. The bilinear WVD has better joint time-frequency resolution than any linear transform. It suffers, however, from a problem of cross-term interference, i.e., the WVD of the sum of two signals is not the sum of their individual WVDs. If a signal contains more than one component in the joint time-frequency domain, its WVD will contain cross terms that occur halfway between each pair of auto-terms. The magnitude of these oscillatory cross terms can be twice as large as the auto-terms. To reduce the cross-term interference, the filtered WVD has been used to preserve the useful properties of the time-frequency transform with a slightly reduced time-frequency resolution and largely reduced cross-term interference. The WVD with a linear low-pass filter belongs to Cohen's class.

### 2.1.3 Cohen's class

The general form of Cohen's class is defined as

$$C(t, \omega) = \int \int s\left(t + \frac{t'}{2}\right) s^*\left(t - \frac{t'}{2}\right) \phi(t - u, t') \exp\{-j\omega t'\} du dt' \quad (3)$$

LINEAR AND NON-LINEAR TIME-FREQUENCY ANALYSIS  
FOR PARAMETER ESTIMATION OF SPACE OBJECTS

TF Transforms	Formula	Kernel
Cohen Class	$C(t, \omega) = \iiint \Phi(\theta, \tau) s\left(u + \frac{\tau}{2}\right) s^*\left(u + \frac{\tau}{2}\right) e^{-j\theta t - j\omega\tau + j\theta u} du d\tau d\theta$	$\Phi(\theta, \tau)$
Wigner-Ville	$WVD(t, \omega) = \int s\left(t + \frac{\tau}{2}\right) s^*\left(t + \frac{\tau}{2}\right) \exp\{-j\omega\tau\} d\tau$	$\Phi(\theta, \tau) = 1$
Choi-Williams	$CW(t, \omega, \sigma) = \iint K_{CW}(u - t, \tau) s\left(u + \frac{\tau}{2}\right) s^*\left(u + \frac{\tau}{2}\right) e^{-j\omega\tau} du d\tau$	$\Phi(\theta, \tau) = K_{CW}(\theta, \tau) = \frac{1}{4\pi^{3/2} \sqrt{\tau^2/\sigma}} \exp\{-\theta^2 \tau^2 / \sigma\}$
Pseudo Wigner	$PWD(t, \omega, \alpha) = \int h(\tau) s\left(t + \frac{\tau}{2}\right) s^*\left(t + \frac{\tau}{2}\right) \exp\{-j\omega\tau\} d\tau$	$\Phi(\theta, \tau) = h(\tau) = \exp\{j\alpha\tau^2/2\}$
Smooth Pseudo Wigner-Ville (SPWV)	$SPWD(t, \omega, \alpha) = \int s(t - u) PWD(t, \omega, \alpha) du$	$\Phi(\theta, \tau) = h(\tau) = \exp\{j\alpha\tau^2/2\}$
Cone Kernel	$CKD(t, \omega) = \iiint K_{CK}(t - u, \tau) s\left(u + \frac{\tau}{2}\right) s^*\left(u + \frac{\tau}{2}\right) e^{-j\omega\tau} du d\tau$	$\Phi(\theta, \tau) = K_{CK}(t, \tau) = \begin{cases} g(\tau); &  t/\tau  < 1/2 \\ 0; &  t/\tau  > 1/2 \end{cases}$

Table 1: *Bilinear Time-Frequency Transforms*

The Fourier transform of  $\phi(t, \tau)$ , denoted as  $\Phi(\omega, \tau)$ , is called the kernel function. It can easily be seen that if  $\Phi(\omega, \tau)=1$ , then  $\phi(t, \tau) = \delta(t)$  and the Cohen class reduces to the WVD. Other types of kernel functions, which lead to the Choi-Williams distribution, the pseudo Wigner, the smoothed pseudo Wigner-Ville and the cone kernel distribution (see Table 1), can be designed to reduce the cross-term interference problem of the WVD [2].

## 2.2 RSO parameters of interest

The radar back-scattering from rotating objects is subject to Doppler modulations that enable us to determine dynamic properties of objects and provide useful information about them. By observing RSOs using a radar, useful parameters for their discrimination can be identified as the rotation period ( $T_\Omega$ ), the maximum Doppler frequency ( $f_{D_{max}}$ ) and the maximum size orthogonal to the LOS( $D_\perp$ ). In particular we can divide them into two categories:

- geometry dependent parameters( $f_{D_{max}}, D_\perp$ )
- geometry independent parameters ( $T_\Omega$ )

The former depend on the acquisition geometry whereas the latter does not.

### 3 Radar Data Simulator

The objective of this section is to define the signal model of the signal received when the radar observe a rotating object. In order to do so we exploit the geometry employed for Inverse Synthetic Aperture Radar (ISAR) technique. The monostatic ISAR configuration will be considered with a brief review of ISAR theory. In particular, will be described system geometry and the received signal model.

#### 3.1 Geometry and signal modelling

Let us consider the simple geometry shown in Figure 3. The monostatic radar consist of a colocated transmitter and receiver (TX/RX) and is located on the origin of the reference system  $T_\xi(\xi_1, \xi_2, \xi_3)$ . The axis  $\xi_2$  is aligned with the radar *Line Of Sight* (LoS).

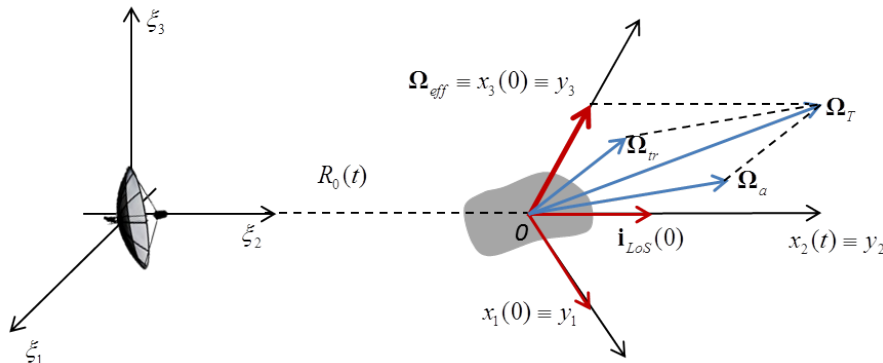


Figure 3: *Monostatic ISAR geometry*

By considering the target as a rigid body, the relative radar target motion can be considered as the superimposition of two contributions: a translation motion and an angular motion which are applied to the center  $O$  of the target. The translation motion is denoted as the *translational rotation vector*  $\Omega_{tr}(t)$ . Note that  $\Omega_{tr}(t)$  is always directed along  $\xi_3$ . The angular motions are represented by the *angular rotation vector*  $\Omega_a(t)$ . The sum of these two rotation vectors yields the *total angular rotation vector*  $\Omega_T(t)$ . The projection of  $\Omega_T(t)$  on the plane orthogonal to the LoS is called the *effective rotation vector*  $\Omega_{eff}(t)$ , it determines the target aspect angle variation exploited in ISAR image reconstruction. As demonstrated in

[3], the plane orthogonal to  $\Omega_{eff}(t)$  is the Image Projection Plane (IPP). The IPP is shown in Figure 4.

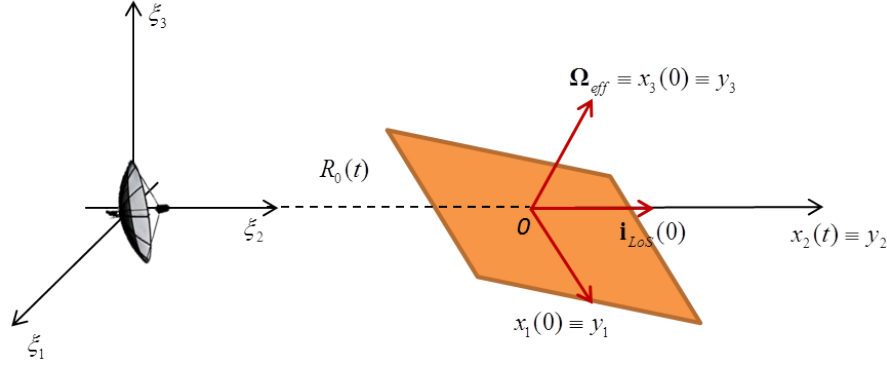


Figure 4: *Image Projection Plane*

Then, a reference system  $T_x(x_1, x_2, x_3)$  is defined, that is embedded in the target and centered in  $O$ . The plane  $(x_1, x_2)$ , whose axes correspond to the cross-range and range coordinates, coincides with the IPP. The axis  $x_2$  is aligned with  $\xi_2$  whereas  $x_3$  with  $\Omega_{eff}(t)$ .

The reference system  $T_x$  is time varying since the effective rotation vector changes its orientation in time. In order to define the reflectivity function of the target, a new reference system  $T_y(y_1, y_2, y_3)$  is defined to be coincident with  $T_x$  at time  $t = 0$ . As it will be clear in the following, the plane  $(y_1, y_2)$  defines the IPP and its axes correspond with the cross-range and range coordinates respectively. In particular,  $\Omega_{eff}(t)$  can be expressed as:

$$\Omega_{eff}(t) = \mathbf{i}_{LoS} \times (\Omega_T(t) \times \mathbf{i}_{LoS}) \quad (4)$$

where  $\mathbf{i}_{LoS}$  is LoS unit vector in the  $T_y$  reference system.

$R_0(t)$  denotes the time varying distance between the radar and the reference point on the target.

### 3.1.1 Received signal

For simplicity, a radar target is represented by a set of point scatterers that are primary reflecting points on the target. The point scattering model simplifies the analysis while preserving

LINEAR AND NON-LINEAR TIME-FREQUENCY ANALYSIS  
FOR PARAMETER ESTIMATION OF SPACE OBJECTS

---

Doppler features. In the simplified model, scatterers are assumed to be perfect reflectors, reflecting all the energy intercepted. As shown in Figure 5 the radar is stationary and located at the origin  $O$  of the radar-fixed coordinate system  $(X, Y, Z)$ . The target is described in a local coordinate system  $(x, y, z)$  that is attached to the target and has translation and rotation with respect to the radar coordinates. The origin  $O$  of the reference coordinates is assumed to be at a distance  $R_0$  from the radar.

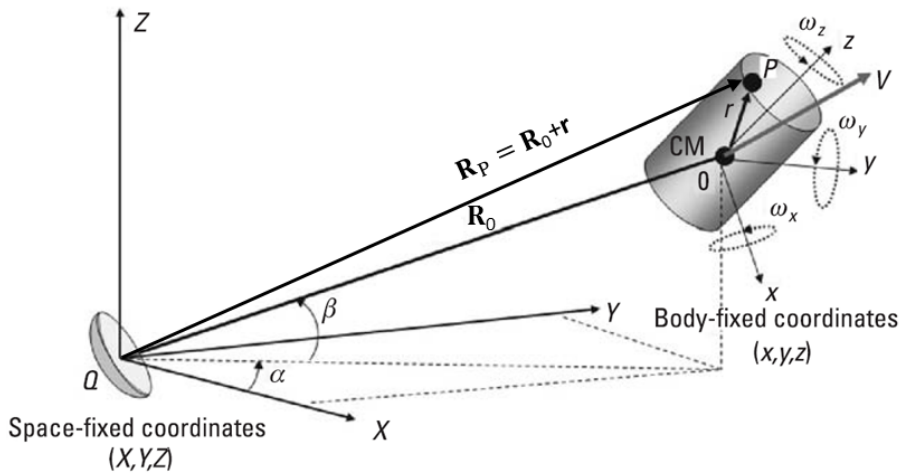


Figure 5: Geometry of the radar and a target with translation and rotation

When radar transmits an EM wave at a carrier frequency  $f_0$ , the received radar signal can be expressed as follows:

$$s_R(t) = s_T(t) \exp \{-j4\pi f_0 R_P(t)\} = s_T(t) \exp \{-j\Phi(t)\} \quad (5)$$

where  $R_P(t) = R_0(t) + r(t)$  is the range from the radar to the scatterer and  $\Phi(t) = -j4\pi f_0 R_P(t)$  is the phase function at time  $t$ . The modulation induced by rotation structure can be regarded as a unique signature of the target. Let us now consider a simple case of a rotating blade where  $\alpha = \beta = 0$  and  $z_0 = 0$  as shown in Figure 6. Where  $\alpha$  and  $\beta$  are the azimuth and elevation angle respectively. Assume a scatterer  $P$  at  $(x_0, y_0)$  on a rotor blade rotates about a center point  $O$  with a rotation rate of  $\Omega$ . The distance from the scatterer to the center point is  $l$ , and the distance between the radar and the center point is  $R_0$ , which may be a function of time if the

target is moving. Assume that at  $t = 0$  the initial rotation angle of the scatterer in the blade is  $\theta_0$ , and at  $t$  the rotation angle becomes  $\theta_t = \theta_0 + \Omega t$  and the scatterer is rotated to  $(x_t, y_t)$ .

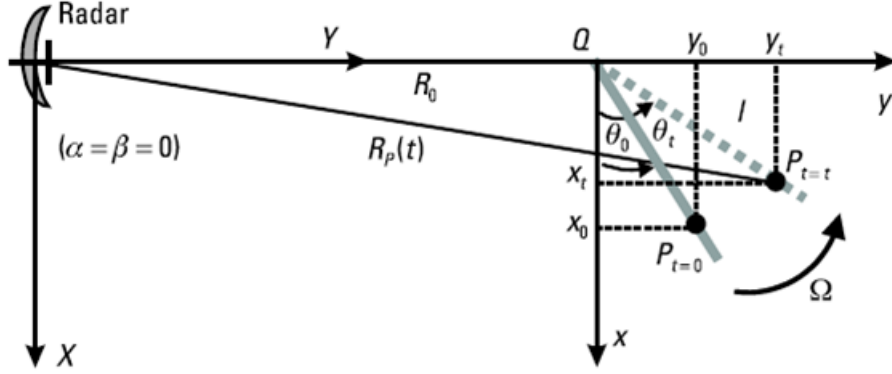


Figure 6: Geometry of the radar and rotor blade when  $\alpha = \beta = 0$

Because we assume both the radar and the rotor are on the same plane, at time  $t$  the range from the radar to the scatterer can be derived as

$$R_P(t) = [R_0^2 + l^2 + 2lR_0 \sin(\theta_0 + \Omega t)]^{1/2} \cong R_0 + vt + l \sin(\theta_0 + \Omega t) \quad (6)$$

where  $v$  is the radial velocity of point  $Q$  and  $(l/R_0)^2 \rightarrow 0$  for far-field. Thus, the radar received signal becomes

$$\begin{aligned} s_R(t) &= \exp \left\{ j \left[ 2\pi f_0 t + \frac{4\pi}{\lambda} R_P(t) \right] \right\} = \exp \left\{ j \left[ 2\pi f_0 t + \Phi_P(t) \right] \right\} = \\ &= \exp \left\{ j \frac{4\pi}{\lambda} [R_0 + vt] \right\} \cdot \exp \left\{ j \left[ 2\pi f_0 t + \frac{4\pi}{\lambda} l \sin(\theta_0 + \Omega t) \right] \right\} \end{aligned} \quad (7)$$

Let  $\theta_0 = 0$ , after compensating the motion and removing the constant phase term in Eq.7, the baseband signal returned from the scatterer  $P$  becomes

$$s_B(t) = \exp \left\{ j \frac{4\pi}{\lambda} l \sin(\theta_0 + \Omega t) \right\} \quad (8)$$

By integrating Eq.8 over the length of the blade  $L$ , the total baseband signal becomes the

following :

$$s_L(t) = L \exp \left\{ j \frac{4\pi}{\lambda} \frac{L}{2} \sin(\Omega t + \theta_0) \right\} \text{sinc} \left\{ \frac{4\pi}{\lambda} \frac{L}{2} \sin(\Omega t + \theta_0) \right\} \quad (9)$$

### 3.2 RSO models

To simplify the problem we modelled targets as a series of point scatterers. The point scatterer model is used under the assumption to observe objects having multiple-structures with size smaller than the sensor resolution. This model, called the point scatterer model, is widely used in many radar application. In fact, the electromagnetic back-scattered signal from a complex target can be thought of as if it is backscattered from a set of scattering centres on the target. As a result, the high resolution of the sensor allows to such points to be mapped as point-scatterers. The point-scatterer model can be related to the electromagnetic scattering theory through high frequency ray optics where a set of highly localized ray phenomena can be related to a reflection or diffraction point on the target. These points can include specular reflections from smooth surfaces, edge diffractions from edge and tips, as well as multiple scattering from dihedral and trihedral corner reflections. An 8-objects database has been built as shown in Figure 7



LINEAR AND NON-LINEAR TIME-FREQUENCY ANALYSIS  
FOR PARAMETER ESTIMATION OF SPACE OBJECTS

---

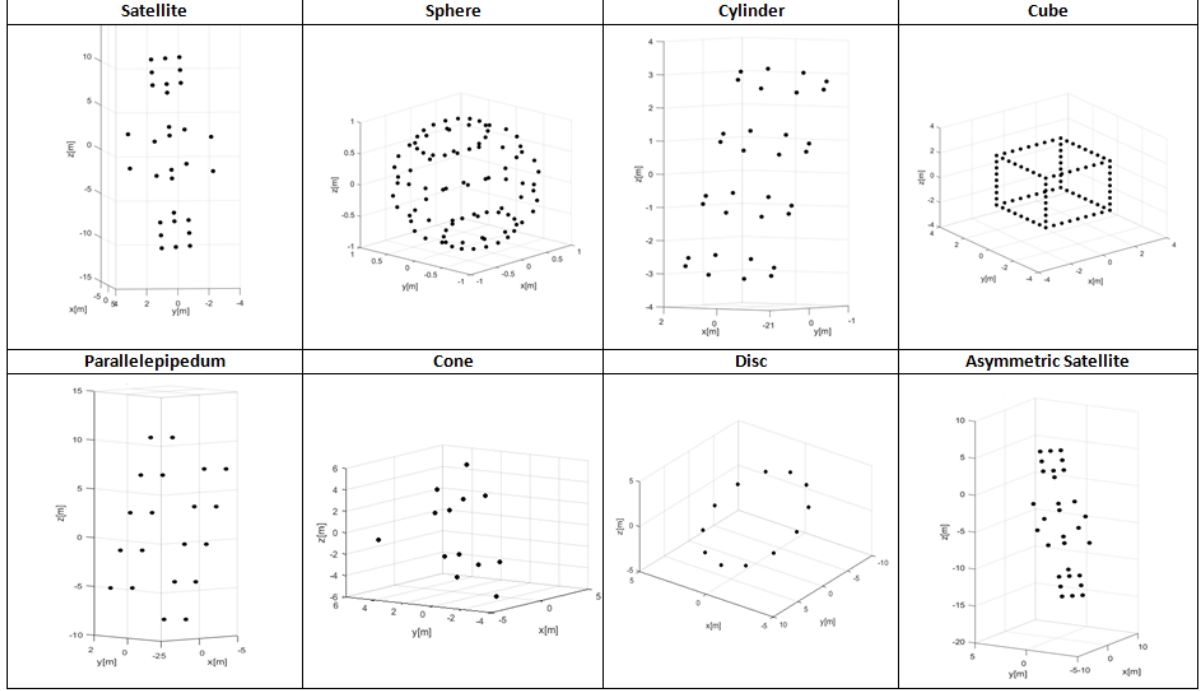


Figure 7: *RSO Database*

## 4 Feature Extraction from radar data

### 4.1 Introduction

If a target moves with a constant rotary motion  $\vec{\omega} = [\omega_x, \omega_y, \omega_z]$ , the instantaneous frequency received will be  $f_i(t) = 2f_0/c[\vec{\omega} \times \vec{r}(t)]\hat{n}$  where  $f_0$  is the frequency of the carrier,  $\vec{r}(t)$  is the distance of one scatterer from the center of rotation and  $\hat{n}$  is the radar-target LOS (Line Of Sight). The amplitude of  $f_i(t)$  depends on the LOS direction: in fact, if  $\hat{n}$  and  $\hat{\omega}$  are parallel,  $f_i(t)$  would be zero despite the target's rotation. The optimal case is when the two vectors are perpendicular to each other since the  $f_i(t)$  is maximum and therefore its measurement is facilitated. The Spectrogram (S) of a rotating rigid-body contains a sinusoid for each scatterer with:

- the same  $T_{\Omega}, \Omega = |\vec{\omega}|$  (because of the rigidity property)
- different amplitudes  $f_D$  depending on their distance from the center of rotation (O)
- different phases according to their position with respect to the radar

Thus, if we estimates one of these sinusoids we can extract the information about  $T_\Omega$  (and so  $\Omega$ ) of the observed RSO. It is clear that the furthest scatterer from O has associated the signature with the highest amplitude in S. By estimating such sinusoid, we obtain also the information about the maximum Doppler frequency ( $f_{D_{max}}$ ). Moreover, if we select the edge signatures, no matter if O is a center of symmetry, it is possible to estimate the maximum dimension of the Object Under Test (OUT). NOTE: with the term maximum we do not refer to the real object but its projection onto the LOS during the Observation Time( $T_{ob}$ ). The worst scenario occurs if  $L\hat{O}S$  and  $\hat{\omega}$  are parallel, in this case the radar does not see the rotation of the RSO and it would not be possible to estimate its size. The Radon transform of a two-dimensional signal containing a two-dimensional delta function is a sinusoidal pattern with amplitude corresponding to the distance of the point from the origin and the initial phase corresponding to the phase of the point position. Therefore, it is obvious that a sinusoidal pattern in the time-frequency plane (produced by a time-frequency representation of sinusoidally modulated signal) will project on a two-dimensional delta in the Inverse Radon Transform (IRT) [4]. By using the IRT on a multi-component sinusoidal signal the energy of each sinusoid is concentrated into a point. The IRT of **S** is evaluated for each element of a vector of angles  $\alpha = \theta_{set} S_f^{opt} = [0^\circ : 0.1^\circ : 360^\circ] S_f^{opt}$ . Among all the IRT computed we pick the one with the highest concentration according to the parameter M. This is done because the points in IRT has the highest concentration when the IRT is calculated using the same number of periods  $S_f$  of the Spectrogram. The Concentration Measure (M)[6] calculated in corrispondence of the i-th  $S_f$  value is defined as follows:

$$\mathbf{IR}_i(p, q) = IRT \left( \mathbf{S}, \theta_{set} \vec{S}_f(i) \right) \quad (10)$$

$$\mathbf{M}_i = \frac{\left\{ \sum_p \left[ \sum_q \mathbf{IR}_i(p, q) + |\mathbf{IR}_i(p, q)| \right]^2 \right\}^2}{\left\{ \sum_p \left[ \sum_q \mathbf{IR}_i(p, q) + |\mathbf{IR}_i(p, q)| \right]^4 \right\}} \quad (11)$$

The best choice according to the concentration criterion is the  $S_f$  that produces the mini-

mum value of M:

$$S_f^{opt} = \arg \min_{\vec{S}_f} \mathbf{M}(\vec{S}_f) \quad (12)$$

Thus,

$$\mathbf{IR}(\mathbf{p}, \mathbf{q}) = \mathbf{IRT}(\mathbf{S}, \theta_{set} \mathbf{S}_f^{opt}) = \mathbf{IRT}(\mathbf{S}, \alpha) \quad (13)$$

where  $\theta_{set}$  is a vector of M equally spaced values between 0 and  $2\pi$  and IR is the IRT of the OUT and will contain a point for every signature. Once we have the IRT of S, we select 2 points  $(k_j, m_j)$   $j=1,2$  that correspond to the extreme of the OUT along the maximum observable size direction. After the selection is done, from the coordinates  $(k_j, m_j)$  of the selected point (SP) we can estimate:

- The modulation amplitude as:

$$A_j = \sqrt{k_j^2 + m_j^2} \quad (14)$$

- The modulation phase as:

$$\phi_j = \arctan(m_j/k_j) \quad (15)$$

- The modulation frequency as:

$$\hat{f}_m = \frac{\alpha}{2\pi} \quad (16)$$

- The rotation period as:

$$\hat{\Omega} = \frac{2\pi \hat{f}_m}{f_s}, \hat{T}_\Omega = \frac{2\pi}{\hat{\Omega}} \quad (17)$$

with  $f_s = M/T_{ob}$

It is then possible to write the correspondent sinusoid:

$$A_j \cos(2\pi \hat{f}_m t + \phi_j) \quad (18)$$

After a scaling transformation we obtain the correspondent sinusoid in the Spectrogram

domain:

$$\hat{f}_{D_{max}}^{(j)} \cos \left( \frac{\hat{\Omega}}{f_s} t + \phi_j \right) \quad (19)$$

- the distance from O to the j-th SP can be written as

$$\hat{D}_{\perp}^{(j)} = \frac{c}{2f_0} \frac{\hat{f}_{D_{max}}^{(j)}}{\Omega} \quad (20)$$

where  $f_0$  is the carrier frequency of the radar.

Finally, the estimation of the maximum dimension of the object is given by:

$$\hat{D}_{\perp} = \hat{D}_{\perp}^{(1)} + \hat{D}_{\perp}^{(2)} \quad (21)$$

## 4.2 Features Extraction Algorithm

The algorithm has been implemented in two versions:

1. Manual mode
2. Automatic mode

## 4.3 Manual Features Extraction Algorithm

### 4.3.1 Functional Block Scheme

In Figure 8 the flow chart of the manual Features Extraction Algorithm mode is depicted. This algorithm mainly consist of 5 steps:

1. Load  $s_R$  of the RSO under test
2. Compute the Spectrogram (S) of  $s_R$
3. Compute the Inverse Radon Transform of  $s_R$
4. Manual selection of the peaks in the Radon Domain

# LINEAR AND NON-LINEAR TIME-FREQUENCY ANALYSIS

## FOR PARAMETER ESTIMATION OF SPACE OBJECTS

---

### 5. Selected Points (SPs) - Features mapping

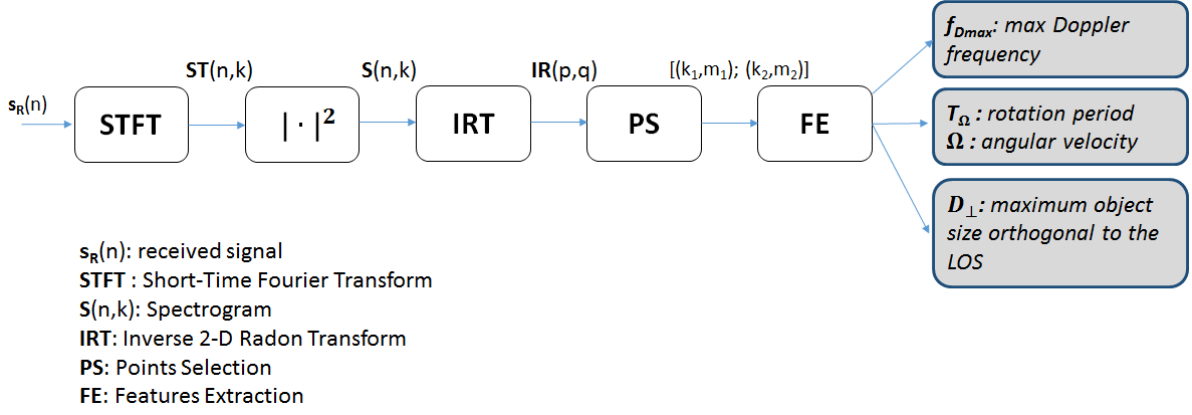


Figure 8: *Features Extraction Alghoritm Workflow*

### 4.3.2 Data Flow

In this section the entire data flow has been inspected. Each processing step will be described in term of four items:

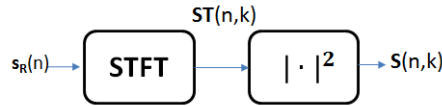
1. Action
2. Motivation
3. Input
4. Output

#### Received signal loading

- **Action:** it allows the user to load the received signal of a particular RSO.
- **Motivation:** load the Received signal of the n-th RSO.
- **Input:** A number (n) that identifies a specific RSO contained in the Database.
- **Output:** Received radar signal ( $s_R$ )

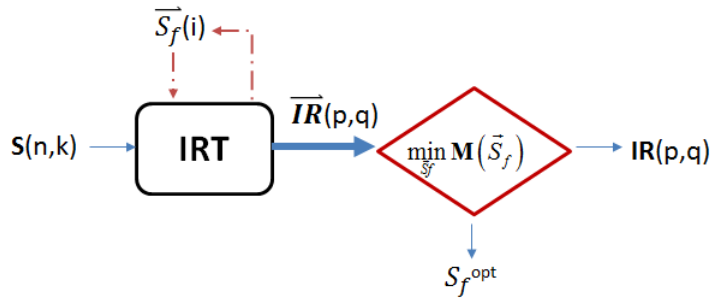
### Spectrogram

- **Action:** The spectrogram  $S$  of the  $s_R$  is computed using the MATLAB built-in function Spectrogram.m, which corresponds to the squared modulus of the STFT of  $s_R$ .
- **Motivation:**  $S$  represents the received signal  $s_R$  in the time-frequency domain where its Doppler signature can be observed.
- **Input:** Received signal  $s_R$
- **Output:** Spectrogram  $S$



### Inverse Radon Transform

- **Action:** The IRT of  $s_r$  is computed using the built-in MATLAB function iradon.m with the optimum value of period of the Spectrogram  $S_f$  defined in Eq. 12.
- **Motivation:** This allows to concentrate the energy of each signature into a point.
- **Input:**  $S$
- **Output:** IRT



### Manual point selection

- **Action:** The user is asked by the machine to select 2 peaks during the script execution:
  - first the user is asked to select the furthest peak from the center (O) of the image IR
  - next is the user asked to select the opposite peak to one selected previously with respect to "O".
- **Motivation:** The furthest peak from O correspond to the scatterer with the highest  $f_D$ , thus the highest distance from O
- **Input:** IRT of the signal
- **Output:**  $(k_1, m_1); (k_2, m_2)$

### SP-features mapping

- **Action:** Using the relationships outlined above (eq. 14-21) we map the selected point in the radon domain into the features space
- **Motivation:** Estimate the features of interest
- **Input:**  $(k_1, m_1); (k_2, m_2)$
- **Output:**  $f_{D_{max}}, D_{\perp}, T_{\Omega}$

## 4.4 Automatic Features Extraction Algorithm

This algorithm is a variation of the version shown in 4.3.

### 4.4.1 Functional Block Scheme

In particular, the manual selection (4.3.2) is replaced by an automatic selection.

The automatic Points Selection (PS) consist of:

LINEAR AND NON-LINEAR TIME-FREQUENCY ANALYSIS  
FOR PARAMETER ESTIMATION OF SPACE OBJECTS

---

1. A thresholding operation
2. 2D peak extraction
3. Refinement of the extracted peaks using their Euclidean distance from O.
4. One of the peaks with maximum Euclidean distance is selected,  $(k_1, m_1)$ .
5. The line "l" that intersects both O and  $(k_1, m_1)$  is used to fill a binary mask such that the line "l" divides the mask in 2 parts, and the part in which  $(k_1, m_1)$  is contained is set to 0. The coordinates of the second peak  $(k_2, m_2)$  are selected after the masking operation.

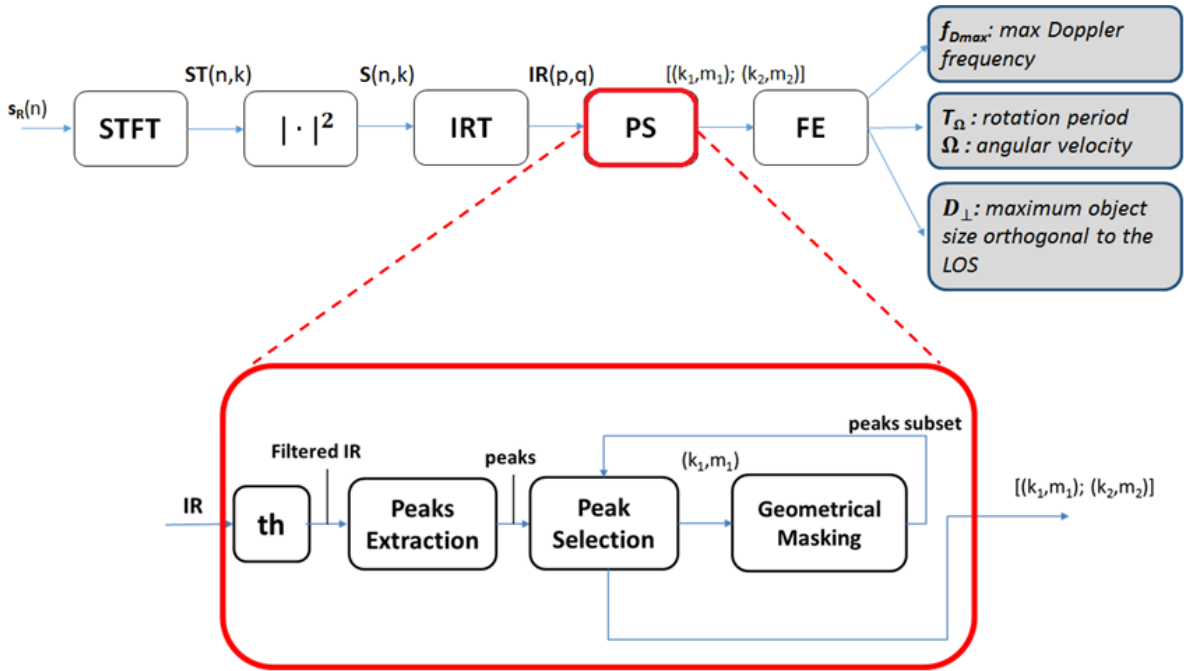


Figure 9: Features Extraction Automatic Algorithm Workflow

#### 4.4.2 Automatic Point Selection Flow

Here, only the PS processing step will be described, since the description of the other parts of the software have already been given in section 4.3.2.

#### Thresholding



- **Action:** it applies a threshold ( $th$ ) to the **IRT** matrix that depends on the mean and standard deviation of the **IRT** map.

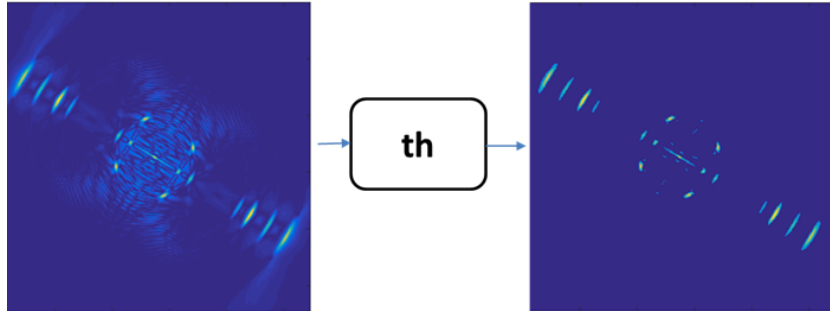
$$th = mean2(|IRT|) + \xi std2(|IRT|), \quad \xi = 3.5 \quad (22)$$

where,

$$mean2(|IRT|) = \frac{1}{N^2} \sum_{i=1}^N \sum_{j=1}^N |IRT_{i,j}| \quad (23)$$

$$std2(|IRT|) = \sqrt{\frac{1}{(N-1)^2} \sum_{i=1}^N \sum_{j=1}^N |IRT_{i,j} - mean2(|IRT|)|^2} \quad (24)$$

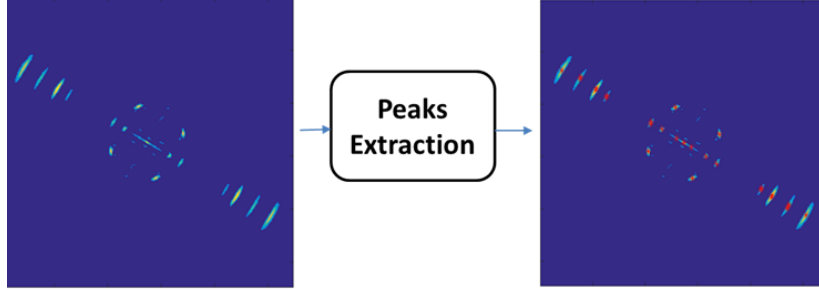
- **Motivation:** it separates the content related to the object from the contribute due to other signal components (such as noise, artefacts and so on).
- **Input:** **IRT**
- **Output:** thresholded **IRT**



## 2D Peaks extraction

- **Action:** find peaks using local maxima
- **Motivation:** the coordinates of each peak in the IRT map are used to define their euclidean metric
- **Input:** filtered **IRT**

- **Output:** a two column matrix of the peaks coordinates, **peaks**=[**x**;**y**]



### Euclidean distance calculation

- **Action:** the Euclidean distance of each SP is computed with respect to the center of rotation O.
- **Motivation:** the euclidean distance is the characteristic of the peak that we need to evaluate which peak is the furthest from "O".
- **Input:** **peaks**
- **Output:** vector of euclidean distances, **eucl<sub>d</sub>** Considering the i-th value of the matrix **peaks** we call  $x_i$  and  $y_i$  its coordinates. Given that, the euclidean distance of the i-th peak is defined as:

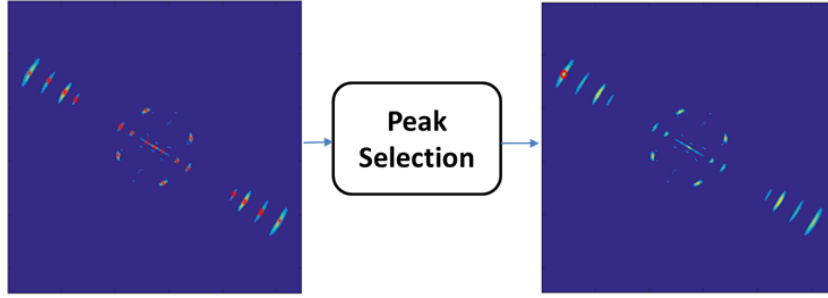
$$eucl_d^{(i)}(x_i, y_i) = \sqrt{(x_i - x_O)^2 + (y_i - y_O)^2} \quad (25)$$

### Peak selection

- **Action:** the peak with maximum euclidean distance is chosen. If more than one peak has the same distance from O, we pick the one with highest amplitude.
- **Motivation:** the peak with maximum euclidean distance from "O" corresponds to the point with maximum Doppler frequency  $f_{D_{max}}$
- **Input:** **eucl<sub>d</sub>**, filtered **IRT**

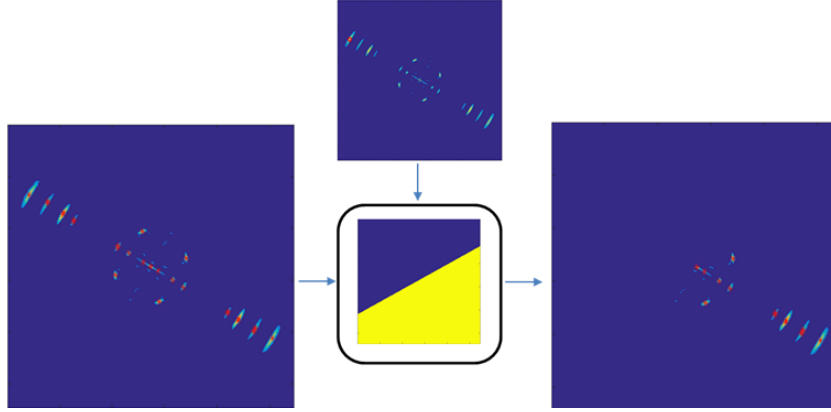
- **Output:**  $(k_1, m_1)$

$$(k_1, m_1) = \arg \max_{x,y} (\text{eucl}_d) \quad (26)$$



### Geometrical masking

- **Action:** It is defined a line  $l$  that intersects  $O$  and  $(k_1, m_1)$ . Using line  $l$  we fill a binary mask such that the line  $l$  divides the mask in 2 parts and the part in which  $(k_1, m_1)$  is contained is set to 0. Then this mask is used to select a subset of the peaks extracted previously.
- **Motivation:** In order to estimate the maximum size of the OUT we also need to find the point of the target that is diagonally opposite to the SP. Our algorithm search for the peak at maximum euclidean distance from  $O$ . Thus, in case of asymmetrical objects if we need to exclude the side of the object where the first detection is located. Otherwise we would estimate the RSO size incorrectly.
- **Input:** peaks, filtered  $IRT, (k_1, m_1), O$
- **Output:** peaks subset



## 4.5 Data Analysis

After describing the Scenario, in section 4.5.1, the results of the technique described in section 4.4 are shown in section 4.5.3.

### 4.5.1 Scenario description

The parameters used to generate the simulated radar signal are shown in table 2. The geometrical and dynamic properties used to create the RSO dataset are outlined in table 3 .

Simulated radar system		
Symbol	Description	Value
$f_0$	<i>Carrier frequency</i>	5 GHz
$B$	<i>Bandwidth</i>	800 MHz
$T_{ob}$	<i>Observation Time</i>	1.4 s
$f_s$	<i>Sampling frequency</i>	13.2 kHz
$T_r$	<i>Pulse Repetition Interval</i>	75.7 $\mu$ s
$T_i$	<i>Pulse Width</i>	1.25 ns

Table 2: *Simulated radar system parameters*

LINEAR AND NON-LINEAR TIME-FREQUENCY ANALYSIS  
FOR PARAMETER ESTIMATION OF SPACE OBJECTS

---

<b>RSO Dataset Geometrical and dynamic properties</b>					
<b>RSO</b>	<b>Shape</b>	<b>Size(<math>x \times y \times z</math>)[m]</b>	<b><math>D_{\perp}</math>[m]</b>	<b><math>f_{D_{\max}}</math>[Hz]</b>	<b><math>T_{\Omega}</math>[s]</b>
1	Satellite	$4 \times 4 \times 22$	22.0907	6614.1043	0.35000
2	Sphere	$2 \times 2 \times 2$	2	449.1096	0.46667
3	Cylinder	$2 \times 2 \times 6$	6.3246	2840.4188	0.23333
4	Cube	$4 \times 4 \times 4$	5.6569	1270.2739	0.46667
5	Parallelepiped	$2 \times 16 \times 4$	18.5536	5369.0052	0.40000
6	Cone	$12 \times 6 \times 12$	12	2245.5482	0.56000
7	Disk	$12 \times 12 \times 0$	12	4491.0965	0.28000
8	Asymmetric Satellite	$4 \times 4 \times 22$	22.114	4799.8502	0.70000

Note: The distance between the radar and each RSO is  $R_0=900$  Km

Table 3: *RSO Dataset Geometrical and dynamic properties*

#### 4.5.2 Performance Metrics

As performance metrics we consider the following:

##### 1. Mean Percentage Error (MPE,%Err)

The Mean Percentage Error is the mean along the number of different realizations of noise  $N_r$  of the magnitude of the difference between the exact value  $a$  of the quantity being forecast and the forecast  $f_r$  divided by the magnitude of the exact value per 100.

$$\text{MPE} = \sum_{r=1}^{N_r} \left| \frac{a - f_r}{a} \right| 100 \quad (27)$$

##### 2. Normalized Root Mean Square Percentual Error (NRMSPE,%NRMSE)

The Root Mean Square Error (RMSE) is a frequently used as measure of the differences between values (sample and population values) predicted by a model or an estimator and the values actually observed.

$$\text{RMSE} = \sqrt{\frac{1}{N_r} \sum_{r=1}^{N_r} \epsilon_r^2} = \sqrt{\frac{1}{N_r} \sum_{r=1}^{N_r} (a - f_r)^2} \quad (28)$$

Normalizing the RMSD facilitates the comparison between datasets or models with dif-

ferent scales.

$$\text{NRMSE} = \frac{RMSE}{a} \quad (29)$$

The NRMSE expressed in percentual form gives the Normalized Root Mean Square Percentual Error (NRMSPE):

$$\text{NRMSPE} = \text{NRMSE} * 100 \quad (30)$$

#### 4.5.3 Estimation results

In table 4 and table 5 are listed the performance metrics (%Err,%NRMSE) of the estimations obtained referring to the scenario introduced in section 4.5.1.

LINEAR AND NON-LINEAR TIME-FREQUENCY ANALYSIS  
FOR PARAMETER ESTIMATION OF SPACE OBJECTS

RSO 1					RSO 2				
		$T_{\Omega}$	$f_{D_{\max}}$	$D_{\perp}$			$T_{\Omega}$	$f_{D_{\max}}$	$D_{\perp}$
<b>SNR=-5dB</b>	%Err	0,412	0,106	0,538	<b>SNR=-5dB</b>	%Err	0,298	6,561	4,649
	%NRMSE	0,426	28,027	0,558		%NRMSE	0,304	28,027	5,554
<b>SNR=0dB</b>	%Err	0,154	0,106	0,311	<b>SNR=0dB</b>	%Err	0,332	8,339	7,687
	%NRMSE	0,159	0,154	0,315		%NRMSE	0,345	8,777	7,965
<b>SNR=10dB</b>	%Err	0,078	0,106	0,243	<b>SNR=10dB</b>	%Err	0,354	17,246	14,805
	%NRMSE	0,079	0,154	0,249		%NRMSE	0,363	17,856	15,432
<b>SNR=20dB</b>	%Err	0,089	0,106	0,252	<b>SNR=20dB</b>	%Err	0,361	18,546	18,038
	%NRMSE	0,089	0,154	0,257		%NRMSE	0,368	18,835	18,325

RSO 3					RSO 4				
		$T_{\Omega}$	$f_{D_{\max}}$	$D_{\perp}$			$T_{\Omega}$	$f_{D_{\max}}$	$D_{\perp}$
<b>SNR=-5dB</b>	%Err	0,064	15,622	30,005	<b>SNR=-5dB</b>	%Err	0,021	3,334	3,416
	%NRMSE	0,077	28,027	36,871		%NRMSE	0,033	28,027	3,470
<b>SNR=0dB</b>	%Err	0,069	0,747	1,132	<b>SNR=0dB</b>	%Err	0,024	3,334	3,424
	%NRMSE	0,081	0,880	1,242		%NRMSE	0,037	3,388	3,477
<b>SNR=10dB</b>	%Err	0,202	0,885	1,252	<b>SNR=10dB</b>	%Err	0,037	3,334	3,375
	%NRMSE	0,209	1,085	1,393		%NRMSE	0,046	3,388	3,427
<b>SNR=20dB</b>	%Err	0,229	0,679	0,904	<b>SNR=20dB</b>	%Err	0,046	3,334	3,366
	%NRMSE	0,233	0,757	0,971		%NRMSE	0,053	3,388	3,417

Table 4: *Performance results (continue in table 5)*

LINEAR AND NON-LINEAR TIME-FREQUENCY ANALYSIS  
FOR PARAMETER ESTIMATION OF SPACE OBJECTS

RSO 5					RSO 6				
		$T_{\Omega}$	$f_{D_{\max}}$	$D_{\perp}$			$T_{\Omega}$	$f_{D_{\max}}$	$D_{\perp}$
<b>SNR=-5dB</b>	%Err	0,035	0,313	0,368	<b>SNR=-5dB</b>	%Err	0,658	1,749	1,228
	%NRMSE	0,044	28,027	0,417		%NRMSE	0,666	28,027	1,239
<b>SNR=0dB</b>	%Err	0,030	0,313	0,363	<b>SNR=0dB</b>	%Err	0,247	1,812	1,642
	%NRMSE	0,032	0,360	0,410		%NRMSE	0,252	1,839	1,661
<b>SNR=10dB</b>	%Err	0,031	0,313	0,365	<b>SNR=10dB</b>	%Err	0,268	1,812	1,621
	%NRMSE	0,033	0,360	0,412		%NRMSE	0,269	1,839	1,639
<b>SNR=20dB</b>	%Err	0,027	0,313	0,360	<b>SNR=20dB</b>	%Err	0,312	1,812	1,581
	%NRMSE	0,027	0,360	0,411		%NRMSE	0,312	1,839	1,596

RSO 7					RSO 8				
		$T_{\Omega}$	$f_{D_{\max}}$	$D_{\perp}$			$T_{\Omega}$	$f_{D_{\max}}$	$D_{\perp}$
<b>SNR=-5dB</b>	%Err	0,055	10,803	18,261	<b>SNR=-5dB</b>	%Err	0,551	0,402	0,513
	%NRMSE	0,073	28,027	21,196		%NRMSE	0,563	28,027	0,569
<b>SNR=0dB</b>	%Err	0,114	0,355	0,371	<b>SNR=0dB</b>	%Err	0,307	0,402	0,509
	%NRMSE	0,117	0,423	0,432		%NRMSE	0,318	0,405	0,532
<b>SNR=10dB</b>	%Err	0,183	0,292	0,405	<b>SNR=10dB</b>	%Err	0,348	0,402	0,485
	%NRMSE	0,184	0,292	0,406		%NRMSE	0,355	0,405	0,518
<b>SNR=20dB</b>	%Err	0,205	0,292	0,428	<b>SNR=20dB</b>	%Err	0,368	0,402	0,465
	%NRMSE	0,206	0,292	0,428		%NRMSE	0,375	0,405	0,501

Table 5: table 4 continued

The worst behaviour is obtained in the case of RSO 2. The reason behind this is to be found in the low value of the Doppler frequency, which is harder to estimate with respect to higher values due to the Doppler quantisation effect. On the other hand, the best behaviour is produced by RSO 1, whose Doppler frequency is the highest.

By looking at tables 4 and 5, and not considering the worst case of RSO 2, we note that except for the case of SNR of -5dB the maximum %Err and %NRMSE do not exceed (0.4,3.4,3.4) respectively for  $T_{\Omega}$ ,  $f_{D_{\max}}$  and  $D_{\perp}$ . Although this is the case of simulated data, these results give some indications about the accuracy and robustness of the parameter estimator with re-



## LINEAR AND NON-LINEAR TIME-FREQUENCY ANALYSIS FOR PARAMETER ESTIMATION OF SPACE OBJECTS

---

spect to input parameters. A more complete analysis of the algorithm performance is given in terms on classification, as it will be shown in sections 7.2 and 7.3.

## 5 Optical Features

In this section, RSO's optical features of interest will be defined and the methodology that is used to extract them from measurements will be outlined. An introduction to photometry will be presented in sec. 5.1, as photometry is generally used to estimate some object parameters such as spin rotation. Next, the software used to simulate optical data, the reference frames used and an analysis of generated data will be described in sec.5.3 and 5.4. A characterization of the noise will be discussed in sec.5.5 and, finally, a summary of radar and optical features is provided in sec. 5.6.

### 5.1 Introduction to photometry

#### 5.1.1 Definitions

Photometry is an optical technique, that consists of measuring the flux of an astronomical object's electromagnetic radiation. At its most basic, photometry is conducted by gathering light with a telescope and then capturing and recording the light energy with a photosensitive instrument (CCD is the most used).

In the last decades, space debris identification and classification has become a critical task in order to prevent collisions in space. Photometry has been significantly used to extract geometric features of this Resident Space Objects (RSOs) and to classify them [14], [13], [12].

Once an optical observation is obtained, a preprocessing operation is carried out, including a masking operation and a calibration. Light curves are extracted from the preprocessed image, which is also called photometric signature, and a RSO classification can be made. These curves represent the magnitude of light flux as a function of time or as a function of phase angle (PA), which is the angle between the light incident onto an observed object and the light reflected from the object.

According to [13] the following classification can be made:

- Canonical Class: if there is a zero PA peak with the brightness decreasing on either side

## LINEAR AND NON-LINEAR TIME-FREQUENCY ANALYSIS FOR PARAMETER ESTIMATION OF SPACE OBJECTS

---

of zero PA in a symmetric and smoothy monotonic manner.

- A2100 Class: if there is a local minimum in brightness at zero PA. On either side, the brightness increases smoothly up to about  $\pm 40^\circ$  PA. At greater phase angles, the brightness again decreases smoothly. Most of these signatures show general but imperfect symmetry.
- Telstar Class: if there is an underlying Canonical signature. However, there are secondary minor brightness peaks (seen mostly in the blue portion of the spectrum) at about  $\pm 40^\circ$  PA.
- BSS702C Class: if there is an underlying Canonical signature. However, there are secondary major brightness peaks at about  $\pm 60^\circ$  PA. The secondary peaks are not only brighter but also broader than in Telstar Class. In this type, the secondary peaks are known to come from solar panel concentrators.

Another classification is described in [14], according to which objects can be classified as:

- Rocket blocks (R/B)
- Abandoned Satellite
- Space debris

According to [14], all Russian R/B observed give practically identical brightness curves with the following characteristic indications for determining their type:

- The shape of a brightness curve represents periodic structure containing two identical peaks on main rotation period divided by antipeaks.
- The Fourier spectrum of a brightness curve contains two main components associated to a rotation period  $T_0$  and to a second order symmetry.

LINEAR AND NON-LINEAR TIME-FREQUENCY ANALYSIS  
FOR PARAMETER ESTIMATION OF SPACE OBJECTS

---

- On some Fourier spectrum curves, a third component of noticeably smaller amplitude is visible. It appropriates to thin structure of peaks on period because of both peaks and antipeaks have forked vertex in this case.

The main characteristic property of nonfunctioning spacecrafts (abandoned satellites) is the violation of their working type of stabilization in orbit. From the point of view of a photometric signature it results in additional periodicity in the variations of brightness for this satellites. Even if the object had earlier spin stabilization the noticeable precession of its rotation axis occurs when objects change their own state. This precession is observed in variations of satellite brightness. Light curves are then used to determine the shape of an object and the attitude (functioning or abandoned). Concerning space debris, is possible to select three main indications, which should be exhibited in photometric observations of this RSOs:

- Rather small visible brightness, which is connected to their small reflecting surfaces.
- Very jagged curve of brightness, connected to the depending of the dissipation diagram of space debris on a phase and aspect angle.
- Very poorly expressed periodicity of brightness change that is characteristic for any kind of rotated gauze structures and small quasi-plane structures.

In [12] a mathematical model of light curves, based on the object shape, is discussed. Particularly, the total brightness of a target object, made up of  $n$  facets, as seen by the observer is given by:

$$L = \sum_{j=1}^n S(\mu, \mu_0, \alpha) \rho_j a_j \quad (31)$$

where  $S$  is the scattering law (or Bidirectional Reflectance Distribution Function, BRDF),  $\rho_j$  is the albedo of the  $j$ -th facet,  $a_j$  is the area of the  $j$ -th facet, and  $\alpha$  is the solar phase angle. The BRDF model determine the way in which light is reflected off of each plate. Each facet

has a surface area, albedo, and surface normal vector, which completely define the shape's reflectance properties. The parameters  $\mu$  and  $\mu_0$  are equal to the dot product of the facet normal vector  $\mathbf{u}_n^B$  with  $\mathbf{u}_{obs}^B$  and  $\mathbf{u}_{Sun}^B$ , respectively. The solar phase angle ( $\alpha$ ) is the observer-target-Sun angle, defined by  $\arccos(\mathbf{u}_{obs}^I \cdot \mathbf{u}_{Sun}^I)$ . The BRDF used in [12] is a combination of Lommel-Seeliger ( $S_{LS}$ ) and Lambert ( $S_L$ ) laws, and is constructed as:

$$\begin{aligned} S(\mu, \mu_0, \alpha) &= f(\alpha)[S_{LS}(\mu, \mu_0) + cS_L(\mu, \mu_0)] = \\ &= f(\alpha)\mu\mu_0\left(\frac{1}{\mu + \mu_0} + c\right) \end{aligned} \quad (32)$$

where  $f(\alpha)$  is the phase function:

$$f(\alpha) = A_0 \exp\left(-\frac{\alpha}{D}\right) + k\alpha + 1 \quad (33)$$

The parameter  $c$  is a weighting factor that determines the contribution of the Lambert scattering law. The phase function is determined by the amplitude and scale length of the opposition effect ( $A_0$  and  $D$ ) as well as the slope of the phase curve ( $k$ ). [12] uses the following parameters:

c	0.1
$A_0$	0.5
D	0.1°
k	-0.5

Table 6: *Parameters used in the BRDF model by [12]*

For SSA purpose two other BRDF model, known as Ashikhmin-Shirley and Cook-Torrance, have been in common use in recent years. They have the advantage of being fast empirical models which incorporate both diffuse and specular reflections. These models are likely to represent typical spacecraft materials more accurately than the Lommel-Seeliger/Lambert scattering law.

Another feature can be extracted from the flux measured, which is the Albedo-area product. In [15] a relationship between Albedo-area and the flux is presented. albedo-Area is the product of the albedo of the object (the ratio of the electromagnetic radiation reflected by an object and the amount that is incident on it) with its area. While albedo-Area (aA) is an intrinsic property of an object, the observed aA of it at any given moment is a projection of its geometry of observation with respect to the source of illumination and the sensor. "Projected" aA of an object, then refers to its observed value based on the current geometry of observation. "Intrinsic" aA of an object refers to its value independently of the geometry of observation.

Considering a surface  $\Delta A$ , flux is defined as the net sum of the energy  $\Delta E$  flowing both inward and outward through  $\Delta A$  over time  $\Delta t$  as  $\Delta E$ ,  $\Delta A$  and  $\Delta t$  tend to zero:

$$f = \lim_{\Delta A, \Delta E, \Delta t \rightarrow 0} \sum \frac{\Delta E}{\Delta A \Delta t} \quad (34)$$

Flux is also related to apparent magnitude (unit-less measure of the brightness of a celestial object relative to that of another celestial object in a certain electromagnetic waveband) as follows:

$$\mathbf{m}_{obj} - \mathbf{m}_{REF} = -2.5 \log_{10} \frac{f_{RSO}}{f_{REF}} \quad (35)$$

Considering a two-facet model, in which an object can be decomposed in a panel component (P) and a body component (B), the projected albedo-Area can be written as follows:

$$\pi \frac{|RS|^2 |OR|^2}{|AU|^2} 10^{\frac{\mathbf{m}_{SUN} - \mathbf{m}_{RSO}}{2.5}} = aA_P \cos(\omega) \cos(\theta) + aA_B \cos(\psi) \cos(\eta) \quad (36)$$

in which:

- $\theta$  is the angle between the observer-RSO vector and the panel normal vector, and it determines the panel's projected area from an observer's point of view.
- $\omega$  is the angle between RSO-Sun vector and the panel normal vector, and it determines

the panel's projected brightness per unit of area.

- is the angle between the RSO-Sun vector and the RSO-Earth vector, and it determines the projected brightness per unit of area of the body's nadir-pointing face.
- $\eta$  is the angle between the RSO-Earth vector and the observer-RSO vector, and it determines the projected area of the body's nadir-pointing face from the observer's point of view.
- $|RS|$  is the RSO-Sun vector length in meters.
- $|OR|$  is the observer-RSO vector length in meters.
- $|AU|$  is the Astronomical unit in meters.
- $A_P$  and  $A_B$  are the areas of panel and body respectively.

## 5.2 Data generation

In order to evaluate the performances of Optical classifiers we want to simulate optical data acquisition. To accomplish this task the Blender software will be used.

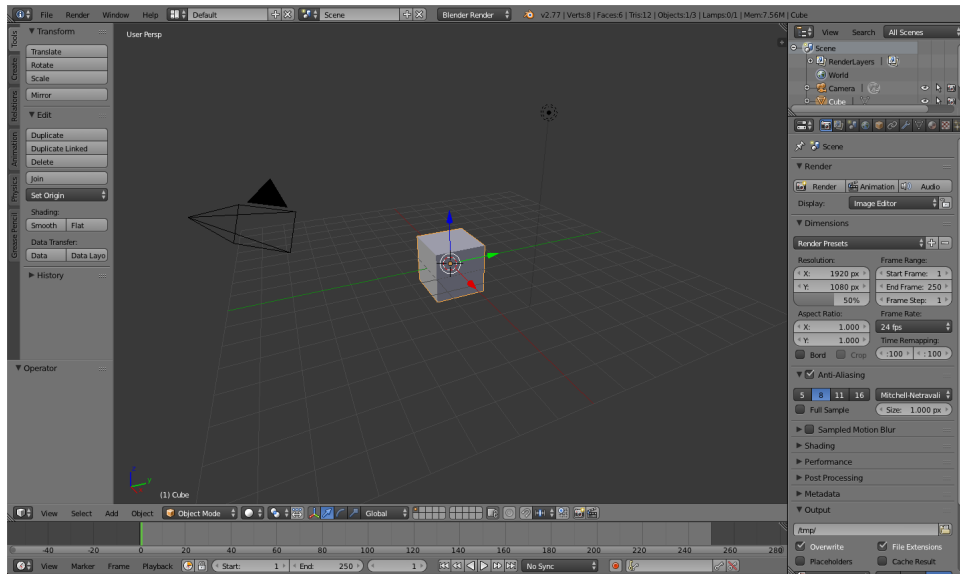


Figure 10: *Blender window with default setup*

## LINEAR AND NON-LINEAR TIME-FREQUENCY ANALYSIS FOR PARAMETER ESTIMATION OF SPACE OBJECTS

---

Blender is a free open source CGI software, which allow to create 3D models of objects and scenes, render images and animations, configuring materials properties such as surfaces reflectivity, light sources and camera motions.

For our purpose we will use Blender to generate the objects listed in Fig. 7. In order to obtain light curves, animation has been generated in which objects have both traslational and rotational motion and the rotation is around a fixed axis. Once obtained a set of frames, each of those has been filtered with a moving-window filter and the relative magnitude of the object is taken.

In the following paragraphs will be discussed: the reference frame used, the generated data analisys and will be characterized the noise of optical measurements.



Figure 11: *Example of optical measurement of satellite object*

### 5.3 Reference frame and measurement units

In this section, the reference frames used for the simulations will be described. For our purposes, we can define two reference frames: the observer's reference frame and the object reference frame. The first one can be used to characterize the traslational motion of the object and the measurements, the second one can be used to characterize the rotational motion of the



LINEAR AND NON-LINEAR TIME-FREQUENCY ANALYSIS  
FOR PARAMETER ESTIMATION OF SPACE OBJECTS

---

object.

The observer's reference frame is chosen so that:

- The origin is on the observer.
- The x-y plane is identified by the azimuthal plane where lies the bisector of the Field of View angle (FOV).
- The x-axis coincides with the bisector of the FOV angle and is positive pointing the object.
- The z-axis is orthogonal to the x-y plane and is positive so that an observer on the z-axis can see the object moving from right to left.

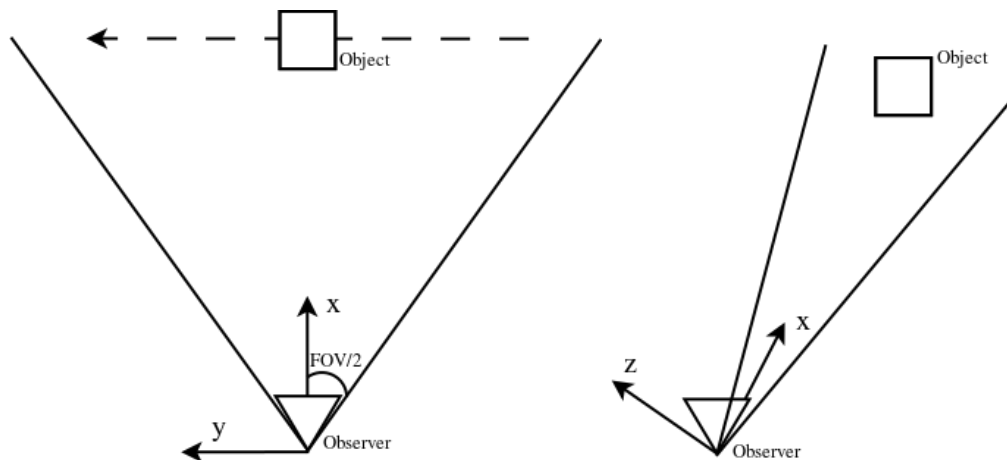


Figure 12: *Observer reference frame*

The object's reference frame is not used for measurement, but is useful to determine the rotation motion at start-up of the simulation. It can be defined as follows:

- The origin is on the center of the object.
- The x-axis is on the side of the object and points on its left.
- The y-axis is on the front of the object.

- The z-axis is on the top of the object.

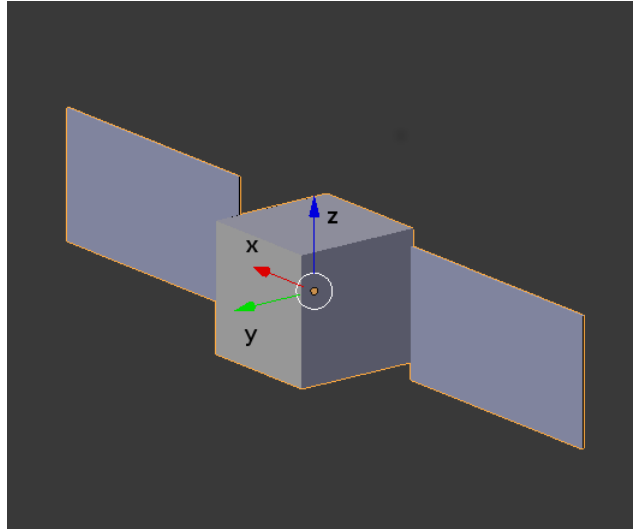


Figure 13: *Object reference frame*

The measurement units used in the simulations are explained as follows. Space is measured, conventionally, in Blender units [BU], which is the unit of measurement used in the software, so velocity is measured in [BU/s]. Angular momentum is measured in [rad/s].

## 5.4 Data analysis

As stated in the last paragraph, a set of light curves are generated using a CGI software. The following cases are analyzed:

1. Cube rotating around his z axis at 3.93 [rad/s].
2. Satellite model rotating around his z axis at 3.93 [rad/s].
3. Satellite model rotating around his z axis at 3.93 [rad/s] observed on a different angle of view respect the precedent simulation.
4. Satellite model rotating around his z axis at 7.85 [rad/s].

LINEAR AND NON-LINEAR TIME-FREQUENCY ANALYSIS  
FOR PARAMETER ESTIMATION OF SPACE OBJECTS

---

5. Satellite model rotating around his z axis at 7.85 [rad/s] observed on a different angle of view respect the precedent simulation.

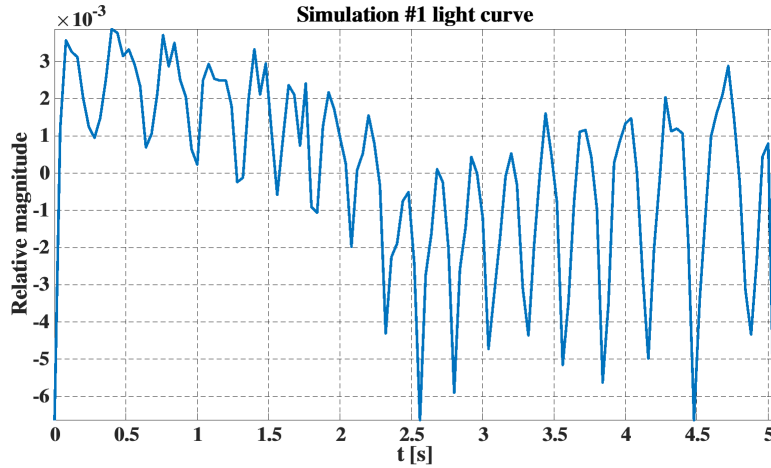


Figure 14: *Simulation #1 light curve*

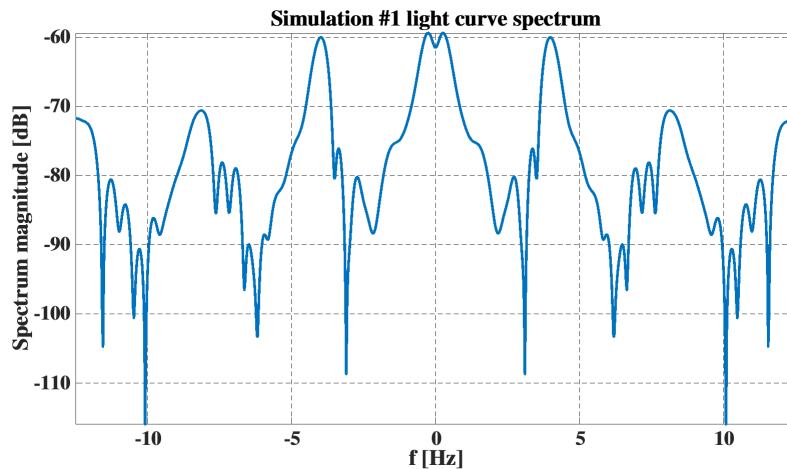


Figure 15: *Simulation #1 light curve spectrum*

Simulated objects have also a traslational motion that is parallel to the observer y-axis at a velocity of 2.5 [BU/s]. Considering simulation #1 the light curve is generated as shown in Fig.14, which has a spectrum shown in Fig. 15. To evaluate the spectrum, a Chebyshev window has been used, in order to reduce SLL. Results of simulations #2 – #5 are shown in Fig. 16 - 23. A first characterization of each object can be made through the light curve spectrm. Considering simulation #2 and #3 it appears that both spectra present the same main

LINEAR AND NON-LINEAR TIME-FREQUENCY ANALYSIS  
FOR PARAMETER ESTIMATION OF SPACE OBJECTS

---

peaks. For this reason observations generated through simulation #2 and #3 are related to the same object. The same considerations can be made on simulation #4 and #5. A comparison between spectra related to different observations of the same object are shown in Fig. 24 and in Fig. 25.

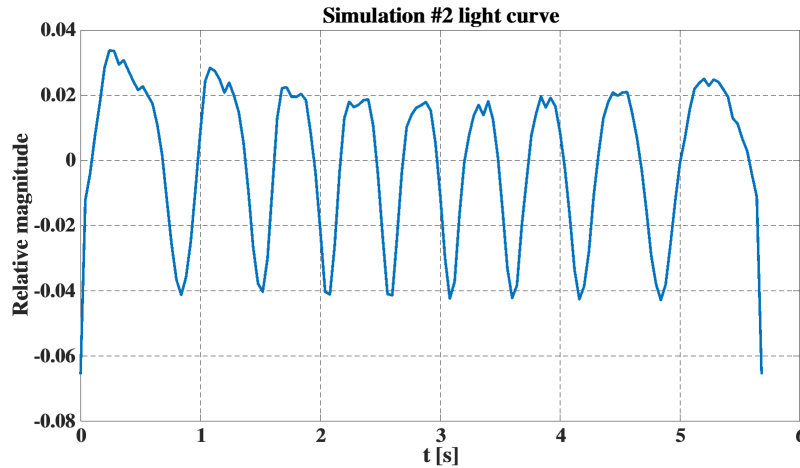


Figure 16: *Simulation #2 light curve*

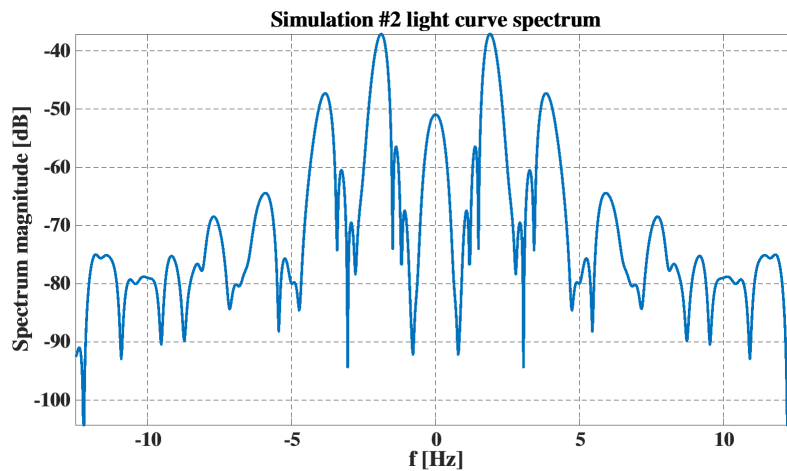


Figure 17: *Simulation #2 light curve spectrum*

These characteristic frequencies are related to the object's rotational speed and to the object geometry. In simulations #4 and #5 the object has a double speed respect to simulations #2 and #3, so the frequencies shown are double. In Fig. 26 a comparison between cube and satellite model used in simulations #1 and #2 is shown. Considering a threshold of -60 [dB] on the spectrum, both have peaks at  $f = \pm 3.8[\text{Hz}]$ , this frequency is relative to the cube

LINEAR AND NON-LINEAR TIME-FREQUENCY ANALYSIS  
FOR PARAMETER ESTIMATION OF SPACE OBJECTS

---

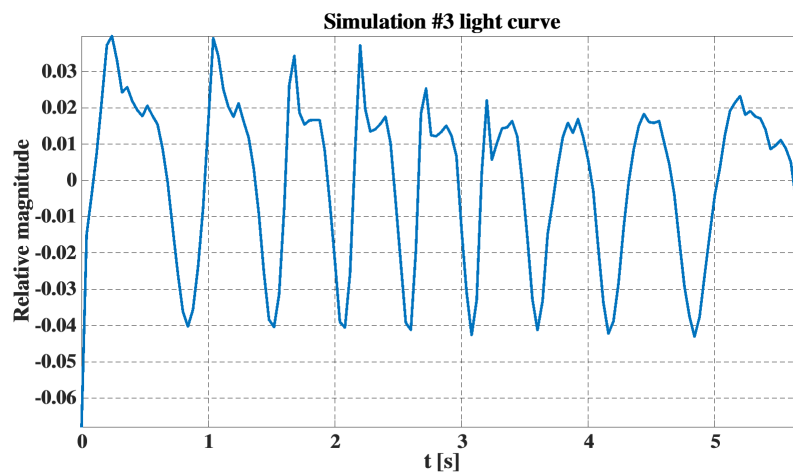


Figure 18: *Simulation #3 light curve*

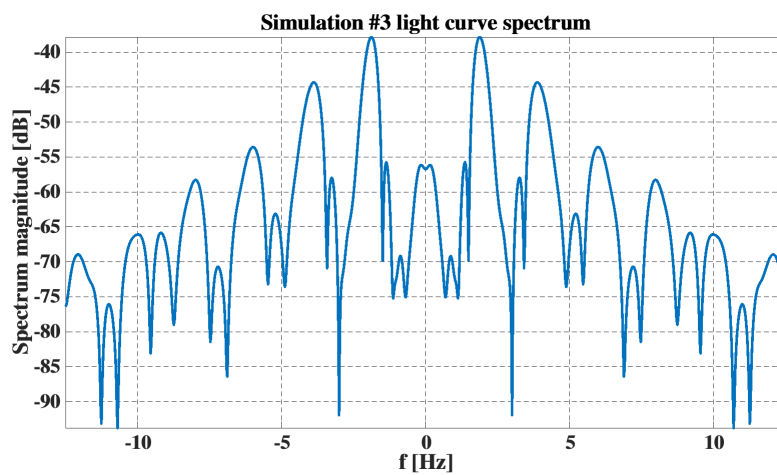


Figure 19: *Simulation #3 light curve spectrum*

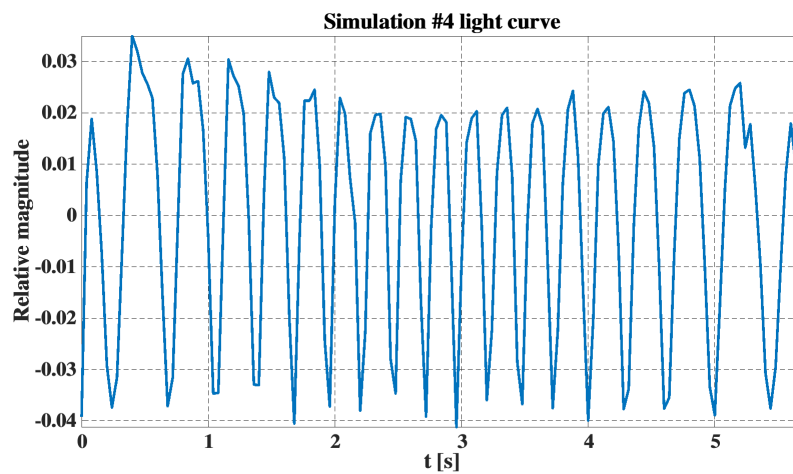


Figure 20: *Simulation #4 light curve*

LINEAR AND NON-LINEAR TIME-FREQUENCY ANALYSIS  
FOR PARAMETER ESTIMATION OF SPACE OBJECTS

---

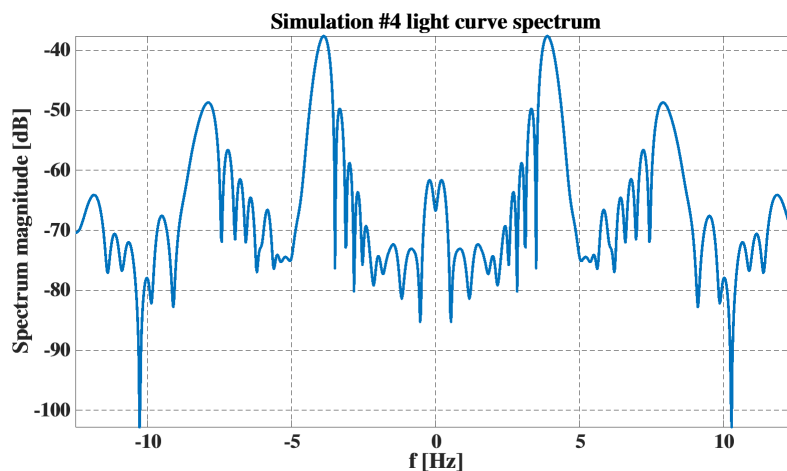


Figure 21: *Simulation #4 light curve spectrum*

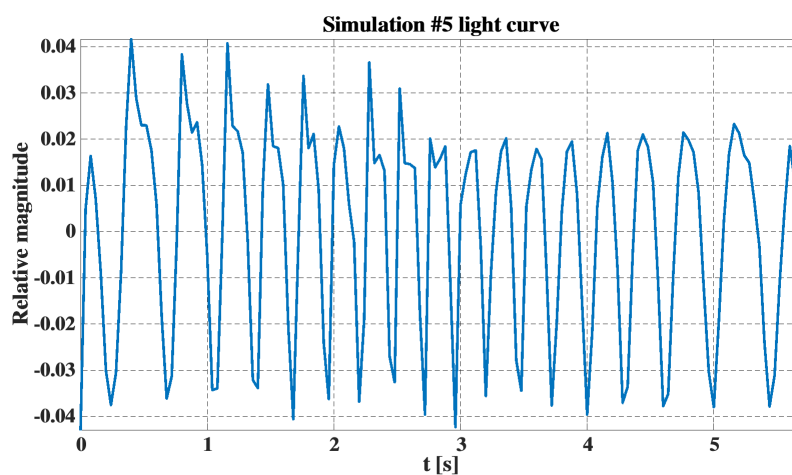


Figure 22: *Simulation #5 light curve*

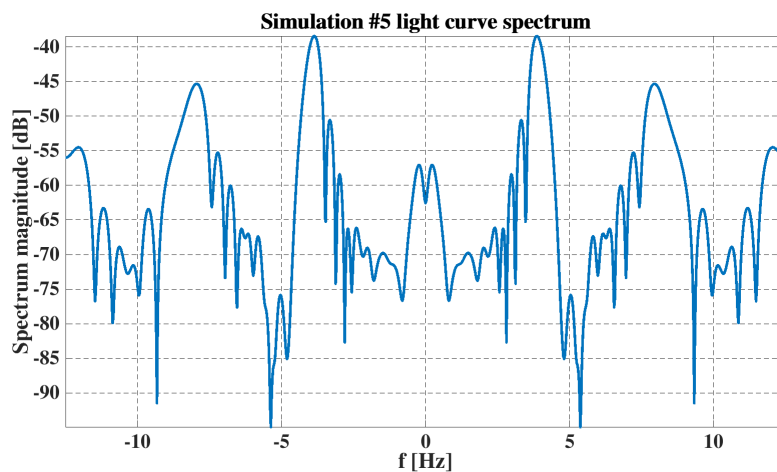


Figure 23: *Simulation #5 light curve spectrum*

# LINEAR AND NON-LINEAR TIME-FREQUENCY ANALYSIS

## FOR PARAMETER ESTIMATION OF SPACE OBJECTS

---

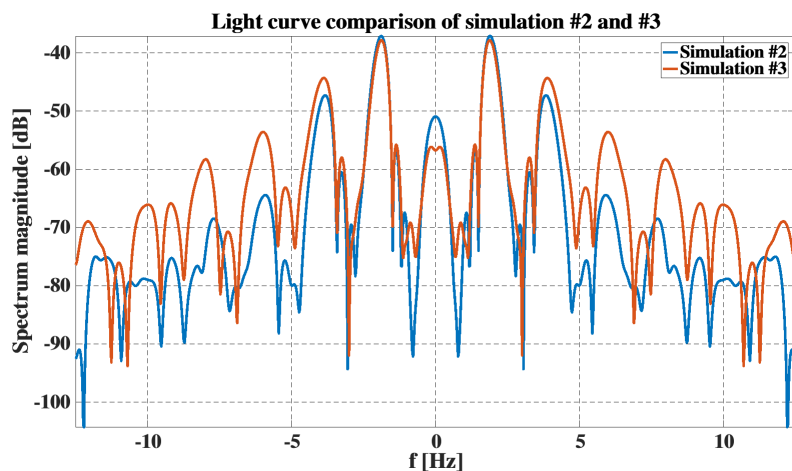


Figure 24: Comparison of light curve spectrums of simulation #2 and #3

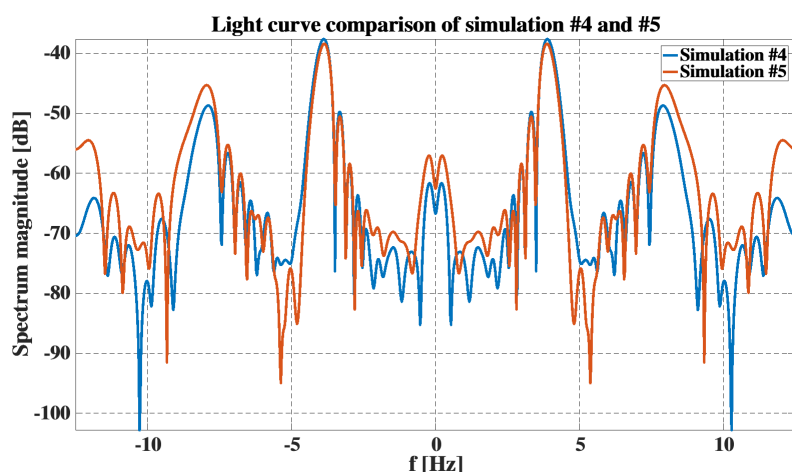


Figure 25: Comparison of light curve spectrums of simulation #4 and #5

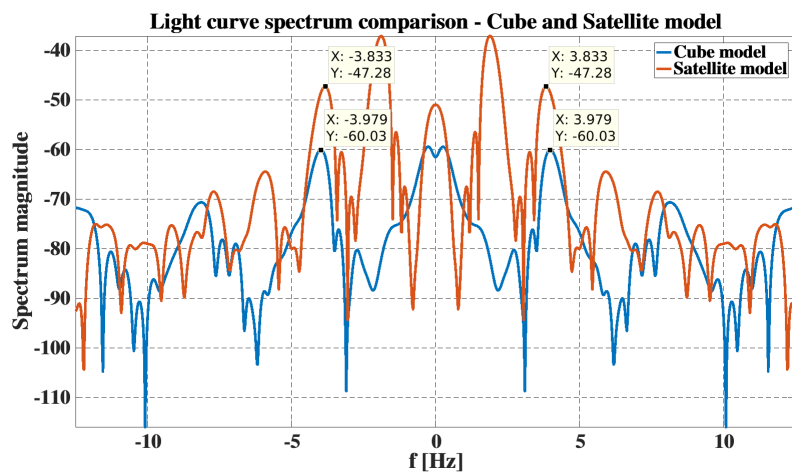


Figure 26: Comparison of light curve spectrums of cube and satellite models

rotational motion and is due to the edge reflection of the cube. Satellite model have also peaks at  $f = \pm 1.88[Hz]$ , due to the motion of the panels. Objects are so characterized by the number of peaks over a threshold and by peak's frequencies.

## 5.5 Noise characterization

In the last paragraph, noiseless measurements have been considered. Noise is composed of undesirable signal components that arise from various sources in an electronic imaging system. The three primary sources of noise in a CCD imaging system are:

- Photon noise
- Dark noise
- Read noise

Photon noise, also known as photon-shot noise, refers to natural variations of the incident photon flux on the device's silicon layer. The number of photoelectrons collected by a CCD pixel exhibits a Poisson distribution and has a square root relationship between signal and noise:

$$N_{ph} = \sqrt{s} \quad (37)$$

where  $N_{ph}$  is photon noise and  $s$  is the signal. This kind of noise cannot be reduced via camera design.

Dark noise arises from the statistical variation of thermally generated electrons within the silicon conducting the CCD. Dark current describes the rate of generation of thermal electrons at a given CCD temperature. Dark noise, which exhibits a Poisson distribution, is the square root of the number of thermal electrons generated within a given exposure time:

$$N_{dk} = \sqrt{Dt_{exp}} \quad (38)$$



where  $N_{dk}$  is the dark noise,  $D$  is the dark current and  $t_{exp}$  is the exposure time. High performance CCD camera systems reduce dark noise by cooling the CCD with thermoelectric coolers (TECs), liquid nitrogen ( $LN_2$ ) or cryogenic refrigeration during camera operations. Read noise ( $N_r$ ) represents the noise introduced during the process of quantifying the electronic signal on the CCD. The major component of the read noise arises from the on-chip preamplifier. Spurious charge also contributes to the overall read noise of the imaging system. HCCD cameras are able to lower read noise by employing carefully designed electronics.

The signal-to-noise ratio for a CCD camera can be calculated as follows:

$$SNR = \int_{\lambda_1}^{\lambda_2} \frac{PQ_e t_{exp}}{\sqrt{(P+B)Q_e t_{exp} + Dt + N_r^2}} d\lambda \quad (39)$$

where:

- $P$  is the photon flux incident on the CCD, measured in [photons/pixel/second].
- $B$  is the background photo flux incident on the CCD, measured in [photon/pixel/second].
- $Q_e$  is the quantum efficiency of the CCD.
- $t_{exp}$  is the exposure time, measured in [seconds].
- $D$  is the dark current, measured in [electrons/pixel/second].
- $N_r$  is the read noise, measured in [electrons rms/pixel].
- $\lambda_1$  and  $\lambda_2$  are the extremes of the wavelength interval considered.

## 5.6 Radar and optical feature summary

Concerning Optical features, the number of peaks in the light curve spectrum are related to the shape of the observed object, such as Albedo-area product. The peak's frequencies in the light curve spectrum are instead related to  $\omega$ , which, as already mentioned, is a geometry

LINEAR AND NON-LINEAR TIME-FREQUENCY ANALYSIS  
FOR PARAMETER ESTIMATION OF SPACE OBJECTS

---

Radar features		Optical features	
Geometry dependent	Geometry independent	Geometry dependent	Geometry independent
$f_{D_{max}}$ $D_{\perp}$	$T_{\Omega}$	Main peak Frequency Number of peaks Peak's frequencies Albedo-area product	$\omega$ Object attitude Object class Object class

Table 7: Radar and optical features

independent feature. Generally speaking, Albedo-area product is an object's intrinsic feature, but its measurement depends on the particular geometry. As stated in section 5.1, the object's attitude is not dependent on the geometry considered and can be estimated directly by means of light curves, and so also the object's class. In order to classify the object as one of the classes defined earlier, the main peak frequency, the number of peaks and the secondary peak's frequencies will be used. The parameter  $\omega$  will not be used because it is a function of both the main peak frequency and of the object's shape. Being the latter an unknown, the estimation of  $\omega$  is not viable. The radar and optical features are summarised in table 7 for the sake of completeness.

## 6 Classifiers Description

The purpose of this section is to describe the classifiers that will be used with the aim to associate a detected object to a certain debris class, or, more precisely, to check if a new detection belongs to the same class of a previous detection after one or more orbit revolutions. Among the many types of classifiers, two have been analyzed in details, namely the Support Vector Machine (SVM) classifier and the Bayesian classifier. While the two classifiers have some differences in the underlying analytical aspects, both focus on building hypersurfaces (or hyperplanes, if the classes are linearly separable) to separate the defined classes with the minimum error possible, or minimum cost achievable. To achieve that, the classifiers act on a hyperspace  $F$  defined by the ensemble of the different features that characterize each classes. In the next paragraph a detailed description of the classifiers' principles are provided.

### 6.1 SVM Classifier

Classifying into  $k$  classes is to find a decision function that assigns each element of the dataset, i.e. each feature vector extracted, to one of the  $k$  classes. In the case of binary classification ( $k = 2$ ) one of the most effective approaches is represented by the Support Vector Machines (SVMs) that will be described below. Starting from binary SVMs is also possible to obtain a classification into  $k$  classes using "voting schemes", or extending their pristine formulation. The following paragraphs will describe these approaches.

#### 6.1.1 Binary SVMs

SVMs were introduced initially by Vapnik [7] in the 80's and represent a very effective technique for non-linear classification. Given a set of input vectors in an  $F$ -dimensional space (where  $F$  is the number of features) the binary classification states that each vector is associated with one of two possible classes. The basic idea of the SVM is to build a hyperplane of separation between the two classes in the  $F$ -dimensional feature space. The training dataset consists of  $\{\mathbf{x}_i, y_i\}$  pairs, where the input vector is  $\mathbf{x}_i \in \mathbb{R}^F$ , and the output is  $y_i \in \{-1, 1\}$ ,

where  $y_i = 1$  identifies the class of positives and  $y_i = -1$  identifies the class of negatives.

### 6.1.2 linear SVM, separable case

The simplest case is that of separable data separable. It is assumed that in the  $F$ -dimensional space exists a hyperplane that can separate all positives from all negatives, as in Figure 27.

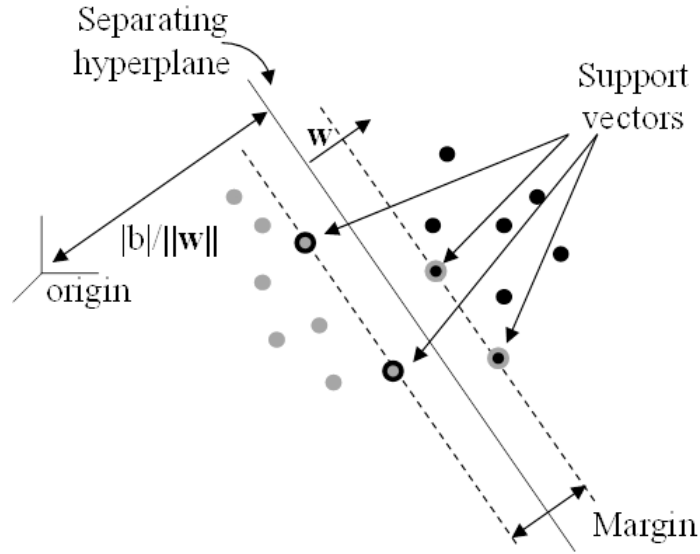


Figure 27: *Separation hyperplane in feature space for separable data*

The hyperplane is identified by the points  $x$  that satisfy the equation  $x \cdot w + b = 0$ , where  $w$  is the normal to the hyperplane and  $b/\|w\|$  is the distance from the origin. The margin is defined as the distance between the positive element nearest to the hyperplane of separation and the negative element nearest to the hyperplane of separation. The algorithm searches the hyperplane of separation with the largest margin. In mathematical terms, the margin is maximized when  $\|w\|^2$  is minimized respecting the constraints for each element:

$$x_i \cdot w + b \geq +1 \text{ if } y_i = +1 \quad (40a)$$

$$x_i \cdot w + b \leq -1 \text{ if } y_i = -1 \quad (40b)$$

i.e.:

$$y_i(x_i \cdot w + b) - 1 \geq 0. \quad (41)$$

The problem can be solved by a Lagrangian formulation, which allows to incorporate the constraints described above in constraints on the Lagrange multipliers ( $\alpha_i$ ) and also permits to show only the scalar products between the training vectors. This allows, in the case of non-linear problems, to use kernel functions that map the data from the original feature space onto a Hilbert space where the problem is linear. The Lagrangian formulation is as follows:

$$L_p = \frac{1}{2} \|\mathbf{w}\|^2 - \sum_i \alpha_i y_i (\mathbf{x}_i \cdot \mathbf{w} + b) + \sum_i \alpha_i \quad (42)$$

then the problem is to minimize  $L_p$  with respect to  $\mathbf{w}$  and  $b$  and simultaneously requesting that the derivatives with respect to all the  $\alpha_i$  (Lagrange multiplier) will be equal to zero, with  $\alpha_i \geq 0$ .

### 6.1.3 linear SVM, non separable case: Cortes-Vapnik formulation

If the data are not separable the method described above does not allow to find a solution. To solve this problem, the constraints should be relaxed so that some errors are tolerated, or some element of the positive class may belong to the half-plane of the negative class and vice versa. The aim is always to maximize the margin and therefore minimize  $\|\mathbf{w}\|^2$  but with the following constraints:

$$\mathbf{x}_i \cdot \mathbf{w} + b \geq +1 - \xi_i \text{ if } y_i = +1, \xi \geq 0 \quad (43a)$$

$$\mathbf{x}_i \cdot \mathbf{w} + b \leq -1 + \xi_i \text{ if } y_i = -1, \xi \geq 0. \quad (43b)$$

The variables  $\xi_i$  are a measure of tolerability. To have a classification error,  $\xi_i$  must exceed unity, then  $\sum_i \xi_i$  represents an upper bound on the training error. The upper limit on the maximum distance between an element and the correct separation hyperplane determines the cost associated with the misclassification of that element. To consider the cost of every classification error, we add a new term to the objective function to be minimized,  $\|\mathbf{w}\|^2/2$ , so the new function to be minimized is:

$$\frac{1}{2}\|\mathbf{w}\|^2 + C \sum_i \xi_i \quad (44)$$

with the constraints in eq. 43, where  $C$  is a parameter to choose: the greater  $C$  is, and the greater the penalty associated to the errors. Incorporating the minimization of the new objective function and constraints, using the Lagrangian formulation we obtain:

$$L_p = \frac{1}{2}\|\mathbf{w}\|^2 + C \sum_i \xi_i - \sum_i \alpha_i [y_i(\mathbf{x}_i \cdot \mathbf{w} + b) - 1 + \xi_i] - \sum_i \mu_i \xi_i, \quad (45)$$

where  $C$  represents an upper limit for the Lagrange multipliers  $\alpha_i$ , while  $\mu_i$  are the Lagrange multipliers which force the positivity of  $\xi_i$ . This formulation of Cortes-Vapnik (also called cost-oriented) [8] makes sure that the optimization process searches a compromise between the margin and the error of misclassification and it is for this reason that for this formulation will be chosen for the problem under consideration.

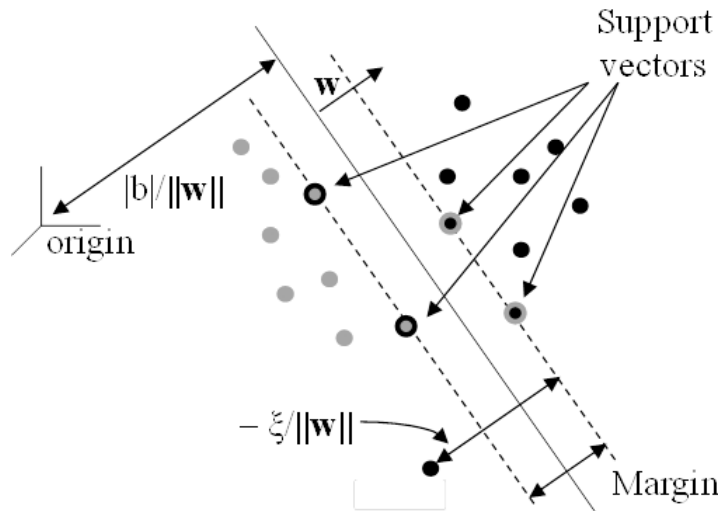


Figure 28: Separation hyperplane in features space for non-separable data

In the event that the decision function is not linear in the space of features, the formulation described above can be generalized using the SVM of kernel functions. Since, as noted above, in the Lagrangian only the scalar products between the vectors of training appears, it is possible to repeat the same treatment also in the nonlinear case as long as the data are mapped into a

Hilbert space  $S$  through a mapping  $\Phi : \mathbb{R}^F \rightarrow S$ . In this way, the training algorithm will depend only from scalar products in  $S$ , or by functions of the form  $\Phi(\mathbf{x}_i) \cdot \Phi(\mathbf{x}_j)$ . Then it can be chosen a kernel function such that  $K(\mathbf{x}_i, \mathbf{x}_j) = \Phi(\mathbf{x}_i) \cdot \Phi(\mathbf{x}_j)$  so that in the algorithm of training appear only  $K$  and not the mapping  $\Phi$ . In this way the problem can be solved in a space of bigger size in which the problem is more linear, and therefore there can be traced back to the case of linear SVM. Examples of kernel functions are the Gaussian kernel:

$$K(\mathbf{x}_i, \mathbf{x}_j) = e^{-\frac{\|\mathbf{x}_i - \mathbf{x}_j\|^2}{2\sigma^2}} \quad (46)$$

or polynomial kernel

$$K(\mathbf{x}_i, \mathbf{x}_j) = (\mathbf{x}_i \cdot \mathbf{x}_j + 1)^p \quad (47)$$

where  $p$  is the degree of the polynomial.

The formulation used for the classification of targets is cost-oriented SVM with Gaussian kernel.

#### 6.1.4 Approaches to multi-class classification

Starting from the combination of multiple SVM binary one can obtain a classification into  $k$  classes [9]. There are two possible approaches:

*one-against-one:*

Are constructed  $k(k-1)/2$  binary SVM classifiers, each trained to distinguish between two classes. Then each classifier is trained with training data from two classes.  $k(k-1)/2$  hyperplanes are constructed which separate each class from each other class. The classification on the test set is made by comparing the results of all classifiers according to a certain voting scheme. For example, the class that receives the highest number of predictions will be the one assigned (max-wins-strategy).

*one-against-all:*

$K$  binary SVM classifiers are constructed, each trained to separate one class from all the others.

Each classifier is trained with the training data from all classes. Then we obtain  $k$  hyperplanes that separate each class from the remaining  $k - 1$  classes. Even in this case the classifiers are then combined by comparing their decisions on a test set according to a voting scheme. The class with the highest decision value will be the one assigned.

There is also a third approach based on a generalized formulation of the algorithm SVM:

*k-class SVM*

This is a generalization of SVM such that the function of decision considers all the  $k$  classes together. The optimization problem then considers the data from all the classes. Despite the number of classifiers needed in the case of the approach one-against-one is greater than the case of one-against-all and formulation of the  $k$ -class (which uses only one), each individual optimization problem is solved in a space of much lower dimensionality, because the training data used for each SVM only come from two classes. Thus the convergence towards the solution is easier in the one-against-one strategy, and also the calculation time is lesser [?].

For these reasons, the approach that has been chosen for the classification of targets is one-against-one.

## 6.2 Bayesian Classifier

In addition to the SVM classifier, also the Bayesian classifier has been analyzed. The Bayesian classifier requires knowledge of some a-priori information, ie the probability of occurrence of a given class ( $c$ ), i.e.  $P(c_i)$ , and the probability of observing a given vector of features  $\mathbf{d}$ , assuming that class has been specified, i.e.  $P(\mathbf{d}|c_i)$ . If such knowledge was perfect, the Bayesian classifier would be optimal, in the sense that the probability of error would be minimal. In practice, however, we do not know either the frequency of the classes or the conditional probability of the features, and it is therefore necessary to estimate these parameters directly from the training data, thus leading to a sub-optimal classifier.

The objective of the classification is to determine the best hypothesis  $h$  within a given space of classes  $H$ , knowing the training data  $\mathbf{d} = [d_1, d_2, d_3, \dots, d_n]$ . In particular, it is required



to determine the most probable hypothesis given the training set  $\mathbf{d}$  plus an a-priori knowledge of the probabilities of the various hypotheses  $h_i$  in the space  $H$  (i.e., the probability of each class). Obviously in the case discussed here, we have no information on the a-priori probability of each class, and it is therefore reasonable to assign to each of them the same value.

Bayes theorem states that

$$P(h_i|\mathbf{d}) = \frac{P(\mathbf{d}|h_i)P(h_i)}{P(\mathbf{d})}. \quad (48)$$

In classification, our interest is to know  $P(h_i|\mathbf{d})$ , the a-posteriori probability, that is, the probability of having a certain class, after looking at the features  $\mathbf{d}$ . Often, a common approach is to proceed with the maximum-a-posteriori (MAP) criterion. In particular,

$$h_{MAP} = \arg \max_{h \in H} P(h|\mathbf{d}) = \arg \max_{h \in H} P(\mathbf{d}|h)P(h) \quad (49)$$

where  $P(\mathbf{d})$  disappears because it does not depend on  $h$ . In our case, where we have assumed all classes equally likely, we can also cancel the term  $P(h)$  and we get a maximum likelihood estimation (Maximum Likelihood, ML).

Under certain conditions it can be shown [11] that every learning algorithm that minimizes the mean square error between the output hypothesis and probabilities on the training data gives out a maximum likelihood hypothesis. The objective of the Bayesian classifier (like that of any classifier) is to determine a particular discriminant function  $g_i : \mathbf{d} \rightarrow \mathbb{R}$  for each  $i^{th}$  class.

As with all kind of real observation, every feature  $\mathbf{d}$  is corrupted by noise. An important assumption is that error has a Gaussian distribution. The choice of Gaussian noise, under the assumption of having many realization in the training set, it is reasonable under the central limit theorem. Otherwise, the performance will be slightly degraded. A training dataset corrupted by Gaussian noise, has the form  $\tilde{\mathbf{d}} = \mathbf{d} + \mathbf{n}$ , where  $\mathbf{d}$  is the noise-free value and  $\mathbf{n}$  is the noise. The simplest and most mathematically tractable formulation is to have lines as objective functions  $g$  of the lines (i.e. the hyperplanes in the case of multidimensional spaces).

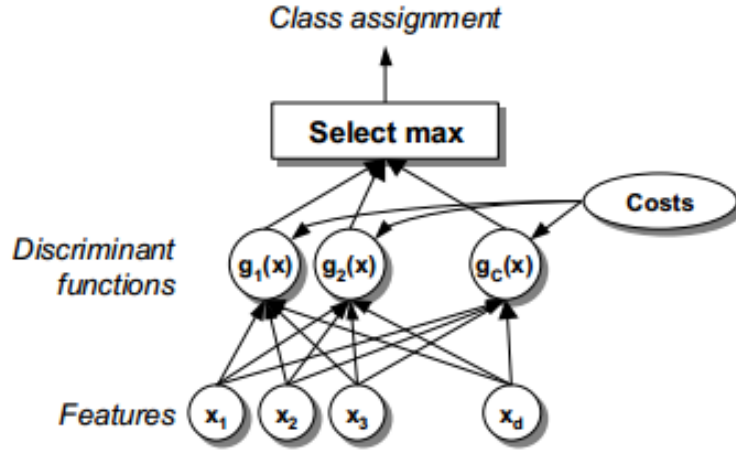


Figure 29: Classifier operation: discriminant function are extracted from features, comparing these values a class can be selected

The underlying assumption in this discussion is that the covariance matrices of the various classes are all equal. Otherwise, the decision boundaries will be quadratic hypersurfaces without changing generality to the approach.

Defined the probability density in the case of multivariate Gaussian noise

$$p_X(\mathbf{x}) = \frac{1}{\sqrt{(2\pi)^N |\Sigma|}} e^{-\frac{1}{2}(\mathbf{x}-\boldsymbol{\mu})^T \Sigma^{-1}(\mathbf{x}-\boldsymbol{\mu})} \quad (50)$$

applying the Bayes rule, the objective function  $g_i(\mathbf{d})$  is no more than the  $P(h_i|\mathbf{d})$ , namely

$$g_i(\mathbf{d}) = P(h_i|\mathbf{d}) = \frac{P(\mathbf{d}|h_i)P(h_i)}{P(\mathbf{d})} = \frac{1}{\sqrt{(2\pi)^N |\Sigma_i|}} e^{-\frac{1}{2}(\mathbf{x}-\boldsymbol{\mu}_i)^T \Sigma_i^{-1}(\mathbf{x}-\boldsymbol{\mu}_i)} \frac{P(h_i)}{P(\mathbf{d})}. \quad (51)$$

In this equation,  $\mathbf{d}$  is the vector of features,  $\boldsymbol{\mu}$  is the average value of features for class,  $\Sigma$  is the covariance matrix of the features for each class, the operator  $|\cdot|$  represents the determinant of the matrix,  $N$  is the number of classes. Back in the conditions of eq. 49, the constant terms  $P(h_i)$  can be removed, having assumed equiprobable classes and  $P(\mathbf{d})$  does not depend on  $h_i$ . Taking the logarithm to obtain a formulation algebraically equivalent but more manageable we

obtain

$$g_i(\mathbf{d})_{\log} = -\frac{1}{2}(\mathbf{x} - \boldsymbol{\mu}_i)^T \boldsymbol{\Sigma}_i^{-1} (\mathbf{x} - \boldsymbol{\mu}_i) - \frac{1}{2} \log |(2\pi)^N \boldsymbol{\Sigma}_i|. \quad (52)$$

This function is the discriminant between classes. At this point the areas of discrimination in the multidimensional space of features  $F$  are obtained in the following manner, as by eq. 49. A point in space  $F$  belongs to a class  $h_i$  if the objective function  $g_i$  for that class assumes the largest value among all the various objective functions.

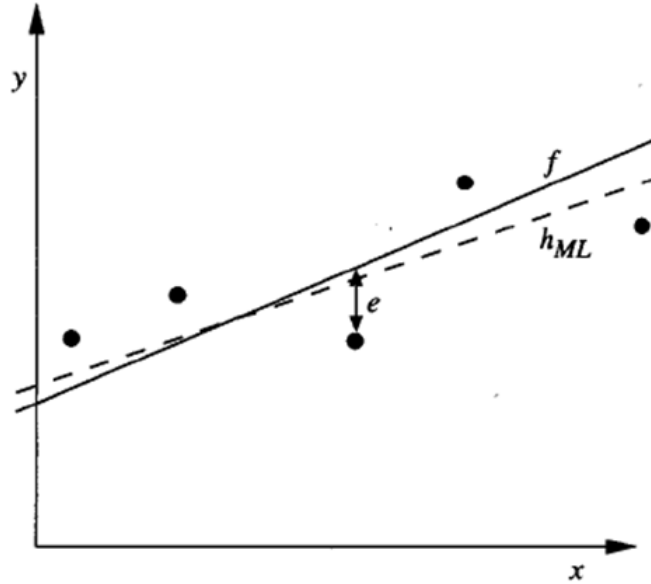


Figure 30: Example for a bidimensional space; line  $f$  represents the linear objective function, line  $h_{ML}$  represents the linear function minimizing the mean squared error. Points in space represent the noise corrupted features.

In the case of equal covariance matrix for each class, i.e.  $\boldsymbol{\Sigma}_i = \boldsymbol{\Sigma}$ , the problem can be further reduced. The second addend in eq. 52 can be eliminated because is the same for all classes, and the discriminant function is reduced to the first term. The expression in the form in eq. 53 is called Mahalanobis distance (or its square). This metric assumes a linear form. Performing the calculations, we have that

$$g_i(\mathbf{d}) = -\frac{1}{2}(\mathbf{d}^T \boldsymbol{\Sigma}^{-1} \mathbf{d} - 2\boldsymbol{\mu}_i^T \boldsymbol{\Sigma}^{-1} \mathbf{d} + \boldsymbol{\mu}_i^T \boldsymbol{\Sigma}^{-1} \boldsymbol{\mu}_i). \quad (53)$$

Removing the first term, which is a constant, we obtain a form of the type  $g_i(\mathbf{d}) =$

LINEAR AND NON-LINEAR TIME-FREQUENCY ANALYSIS  
FOR PARAMETER ESTIMATION OF SPACE OBJECTS

---

$w_1^T \mathbf{d} + w_0$ . In the case of covariance matrix equal to the identity, this distance is the (squared) Euclidean distance. Minimizing this term means therefore minimizing the mean square error. Also, since this term has a negative sign, one must search for its maximum instead.

The Bayesian classifier is natively designed work with multi-class, and is the approach that has been chosen in this report.

## 7 Performances Analysis

The performances of the classifiers are shown in this section. The performances are evaluated and tested considering radar-only features, optical-only features and a fusion dataset comprising the features obtained with both sensors types. The various datasets are created with different Signal to Noise ratios in order to appreciate variations of classification performances, if any. The performances are evaluated separately for Bayesian Classifier and SVM Classifier. In the case of fused dataset, the used approach was the fusion-of-features rather than fusion-of-decisions. Some considerations must be made regarding the fusion datasets. The SNR of the two dataset are derived from two different sensors, so it is impossible to merge directly two different types of dataset (optical vs. radar). Nevertheless, it is possible to perform a comparison by using a combination of the various SNRs in order to obtain couples of optical-radar SNRs, thus obtaining a 2D performance map rather than a 1D graph. In this condition is it possible to better appreciate the classification performances.

The classification approach is based on a one-vs-one strategy. Given a set of possible classes, the objective of the decision process is to know if a specific detection matches the previous detection for a specific class, or not. With this approach, we have a binary decision process (the present detection matches/does not match the previous detection. In an operative scenario, if the match is true, the track is maintained, otherwise a new track is initialized.

The test was performed for each of the 8 classes versus the rest of the possible observations, which we consider as "unknowns". The same training and testing procedures were performed with Bayesian and SVM classifiers. The performances were measured in terms of Probability of Correct Classification ( $P_{CC}$ , blue line), Probability of Missed Classification ( $P_M$ , black line) and Probability of False Alarm ( $P_{FA}$ , red line).  $P_{CC}$  is calculated by counting the occurrences for which the desired target was correctly detected plus the occurrences for which the unknowns were classified as unknowns.  $P_M$  is calculated by counting the occurrences for

which the desired target was classified as an unknown, whereas  $P_{FA}$  is calculated by counting the occurrences for which an unknown is classified as the target. Based on these considerations, it can happen that even with a  $P_{CC}$  of more than 80%, because we correctly classified the unknowns, we can obtain a 100%  $P_M$  because we completely missed the desired target. Due to the number of tests performed, the  $P_{CC}$  resolution is 0.5%, the  $P_M$  resolution is 4% and the  $P_{FA}$  resolution is 0.57%.

## 7.1 Optical Only

The performances obtained with the use of optical features only are shown in this section.

To create the dataset, the simulations were performed with 9 different SNRs. The lowest SNR is 20 dB while the highest is 60 dB. The SNR step is 5 dB; For each SNR, 25 realizations per class are created. For the optical case, a feature selection must be performed based on their characteristics. More specifically, there are classes that have a different number of features with respect to the others, namely the number of frequencies associated with peaks found in a spectrum. Depending on the target, a number up to 12 frequencies may be found for a class, whereas other classes may have only one or two. This differences in the number of peaks create issues with the definition of the classifier, which expects a preset number of features at its input. On the other hand, there are some features that do not suffer of this problem, such as the number of peaks and the main peak frequency, which are single valued features for each object. Therefore, by using only a reduced feature ensemble, the inner separability of the features is not compromised, while facilitating the classification task. The features taken into consideration are:

- dominant peak frequency
- number of peaks [discrete]
- first peak frequency.

# LINEAR AND NON-LINEAR TIME-FREQUENCY ANALYSIS

## FOR PARAMETER ESTIMATION OF SPACE OBJECTS

To perform the classifiers' training, a single SNR was chosen, namely 45 dB, which is an intermediate value between the lowest and the highest. It has to be noted that the test was performed also with the 45 dB set. The test is not unnecessary, because the training algorithm does not produce hypercurves that perfectly separates features, rather it designs hypercurves that minimize the mean square error (MSE). In fact, it is possible to obtain some classification error even when the SNR of the train set and the SNR of the test set match.

Figures 31 from 38 show the results for each of the eight target types obtained with a Bayesian classifier.

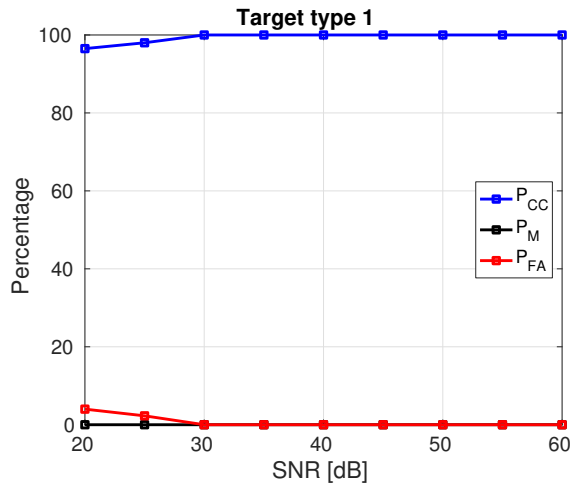


Figure 31: Bayesian, Target 1

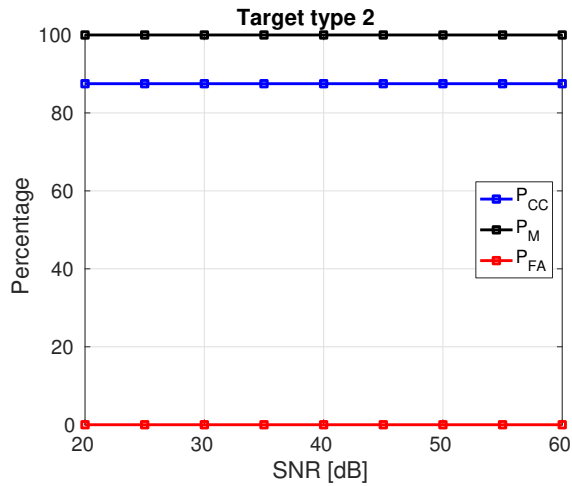


Figure 32: Bayesian, Target 2

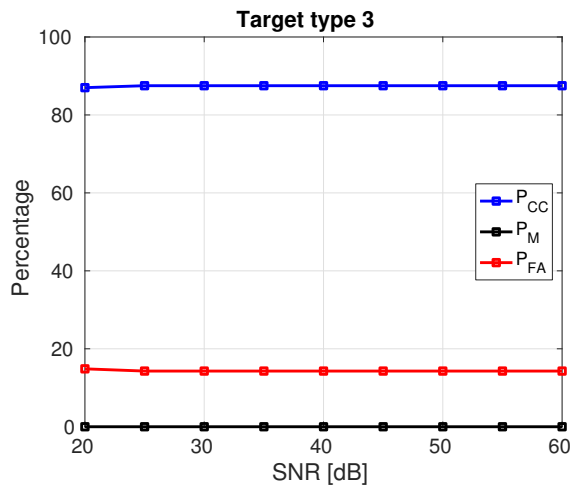


Figure 33: Bayesian, Target 3

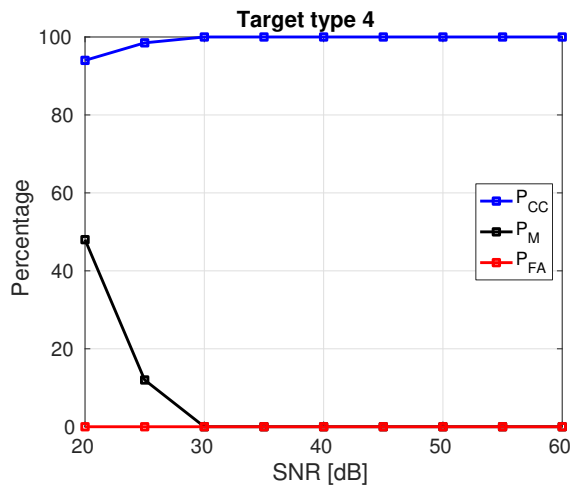


Figure 34: Bayesian, Target 4

LINEAR AND NON-LINEAR TIME-FREQUENCY ANALYSIS  
FOR PARAMETER ESTIMATION OF SPACE OBJECTS

---

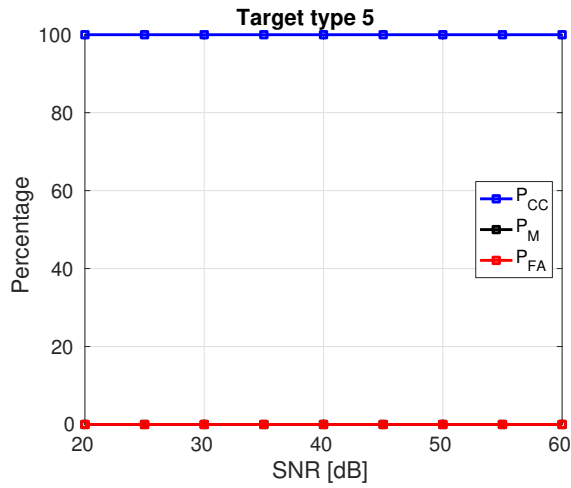


Figure 35: Bayesian, Target 5

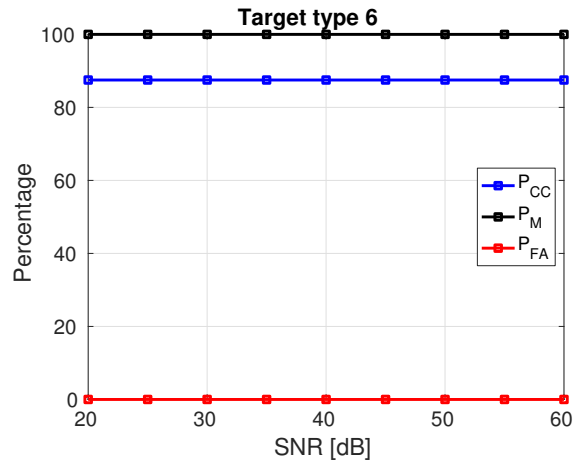


Figure 36: Bayesian, Target 6

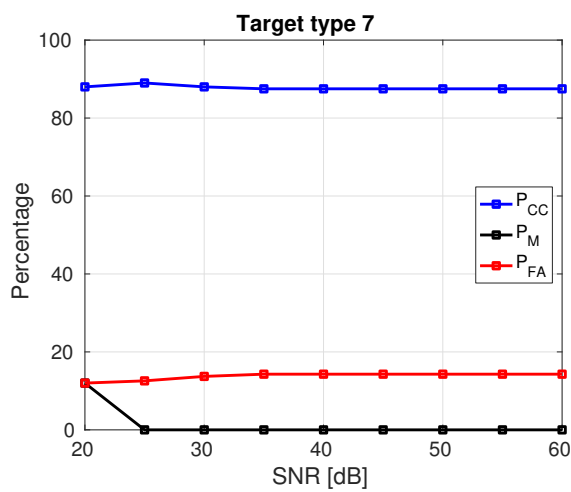


Figure 37: Bayesian, Target 7

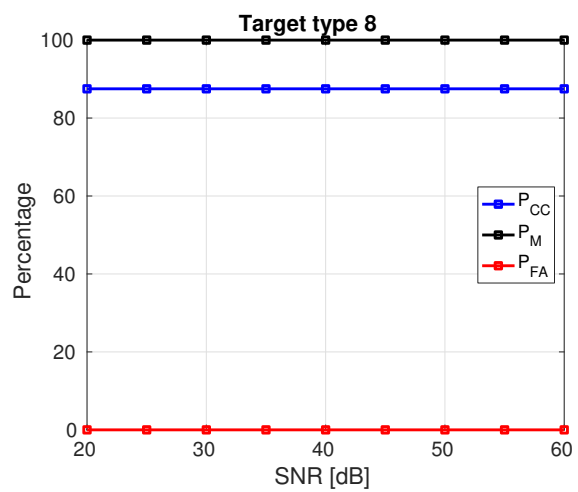


Figure 38: Bayesian, Target 8



# LINEAR AND NON-LINEAR TIME-FREQUENCY ANALYSIS

## FOR PARAMETER ESTIMATION OF SPACE OBJECTS

---

The results that we obtain with the Bayesian classifier can be either very good or very bad, depending on the target under observation. While the performances are nearly independent of the SNR, due to the fact that the features are quite separable in the feature hyperspace, results are not very satisfying. Only Target 1, Target 3, Target 5 and Target 7 show good performances, save for a not negligible  $P_{FA}$  for Target 3 and Target 7. In the other cases, the target is completely missed. The partial conclusion is that with optical-only features in combination with a Bayesian classifier the results are not encouraging although some slight improvement may be achieved by tuning the classifier.

Figures 39 from 46 show the results for each of the eight target types obtained with the SVM classifier.

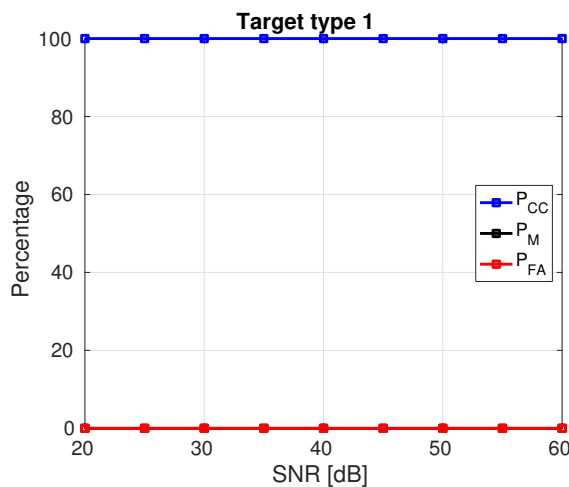


Figure 39: SVM, Target 1

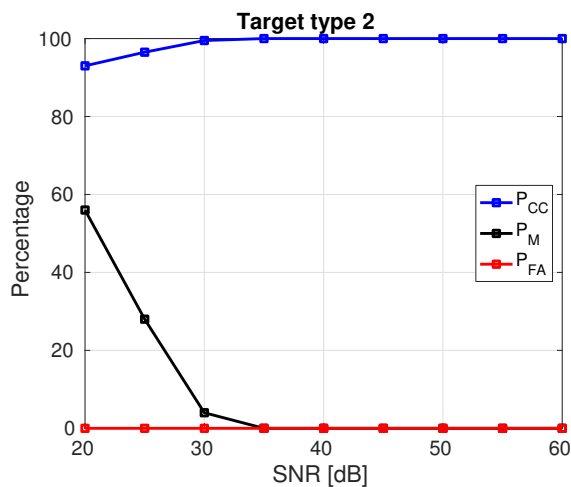


Figure 40: SVM, Target 2

LINEAR AND NON-LINEAR TIME-FREQUENCY ANALYSIS  
FOR PARAMETER ESTIMATION OF SPACE OBJECTS

---

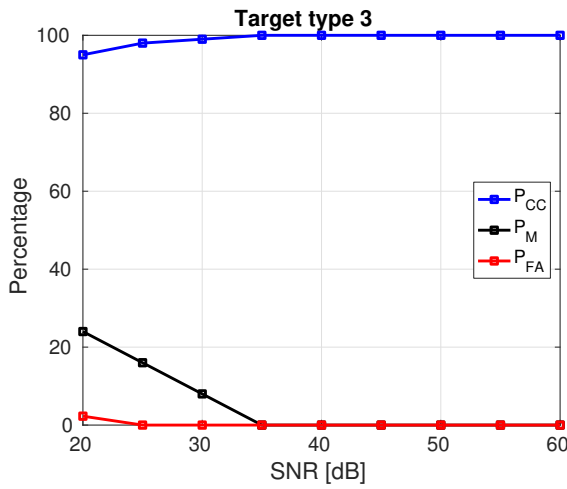


Figure 41: SVM, Target 3

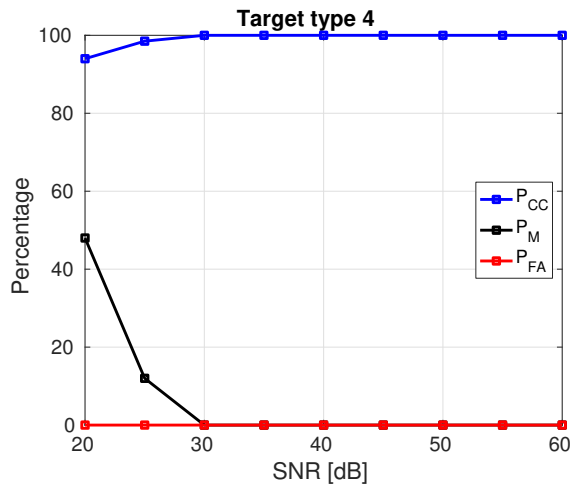


Figure 42: SVM, Target 4

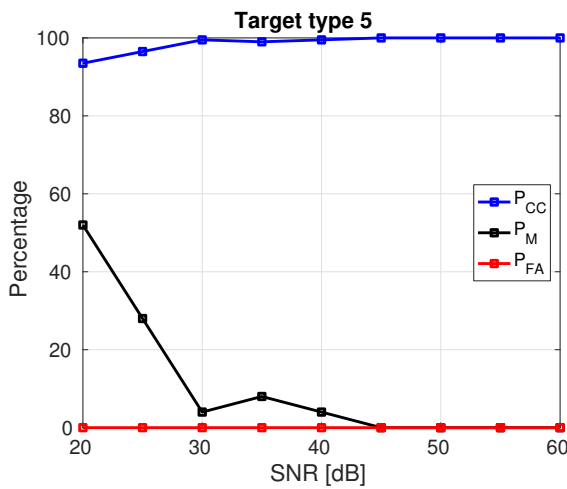


Figure 43: SVM, Target 5

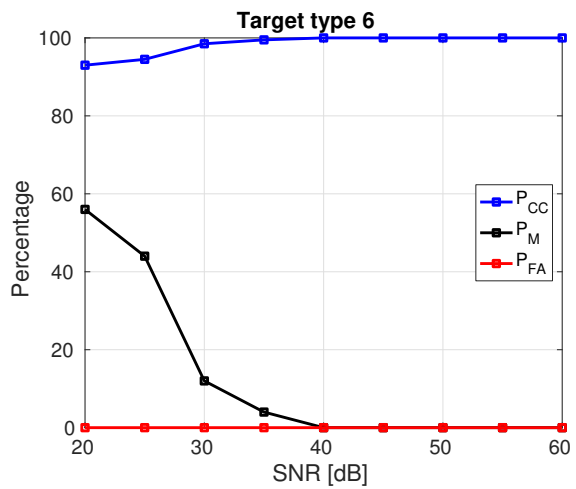


Figure 44: SVM, Target 6

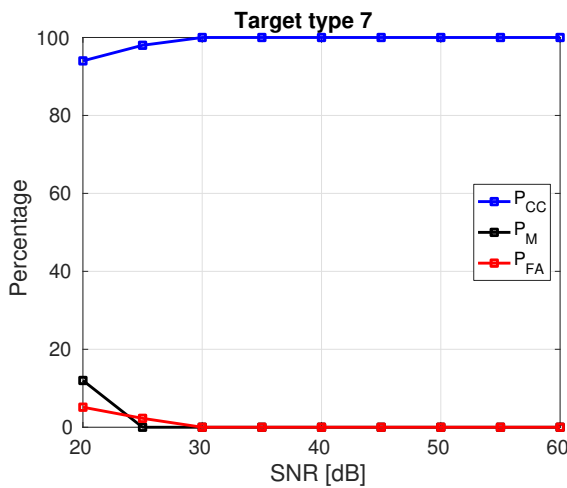


Figure 45: SVM, Target 7

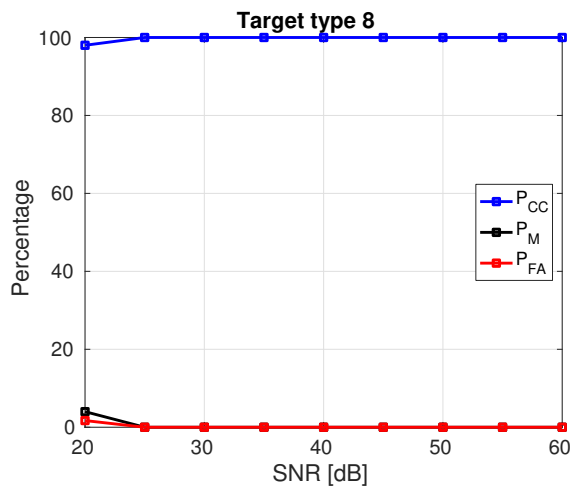


Figure 46: SVM, Target 8

The results that we obtain using the SVM classifier with optical features are better. The various targets are always correctly classified when the SNR is higher, while the  $P_M$ , while being high for the lowest SNR, decreases with increasing SNR. The  $P_{FA}$  is low enough, with the highest being 8% for Target 7 at the lowest SNR.

In conclusion, the simulations suggest that if we have only optical data, the SVM classifier produces better results than the Bayesian, indicating that the information in the optical data may be sufficient to produce acceptable results.

## 7.2 Radar Only

In this section the performance obtained with the use of radar features only are listed.

To create the dataset, the simulations were performed with 4 different SNRs, which are -5 dB, 0 dB, 10 dB and 20 dB. For each SNR, 25 realization per class are performed. For the radar case we utilized all the three extracted features, therefore a feature selection was not performed. This means that the extracted features result in a high separation in the features hyperplane, and that all the features are present for every class. The features taken into consideration are:

- maximum spectrogram Doppler frequency
- maximum object size, projected orthogonally to the LOS
- rotation period

To perform the classifiers' training, a single SNR was chosen, namely 0 dB. It has to be noted that the testing was performed also with the 0 dB set. As in the case of optical data and for the same reasons, the test is not unnecessary. So, also in this case, it is possible to obtain some classification errors even when the SNR of the train set and the SNR of the test set match.

Figures 47 from 54 show the results for each of the eight target types obtained with Bayesian classifier.

LINEAR AND NON-LINEAR TIME-FREQUENCY ANALYSIS  
FOR PARAMETER ESTIMATION OF SPACE OBJECTS

---

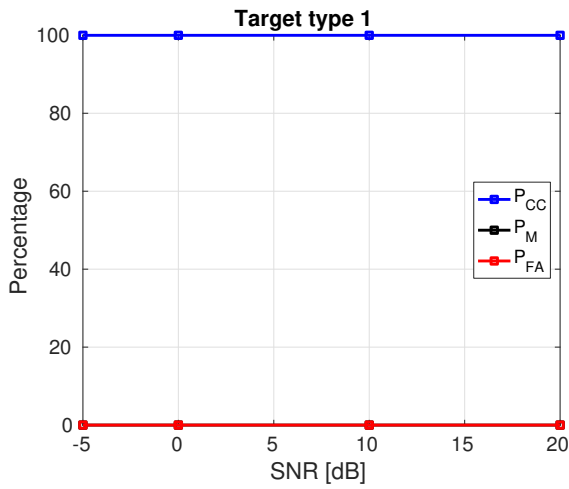


Figure 47: Bayesian, Target 1

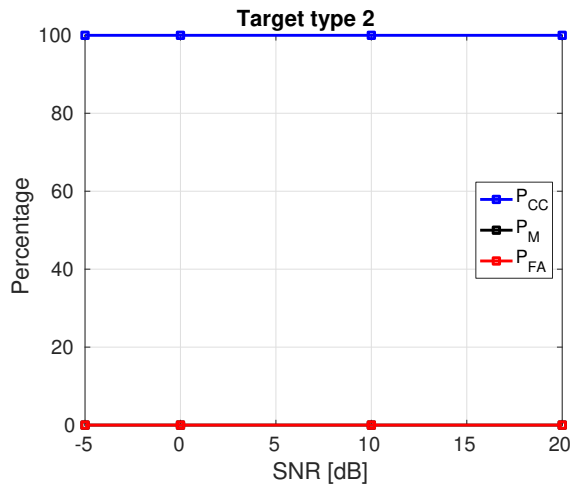


Figure 48: Bayesian, Target 2

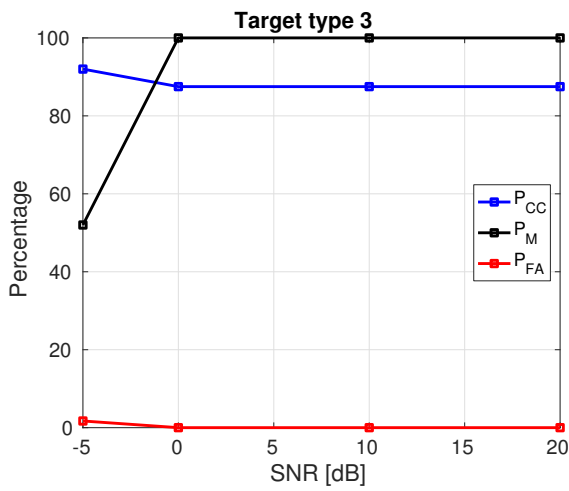


Figure 49: Bayesian, Target 3

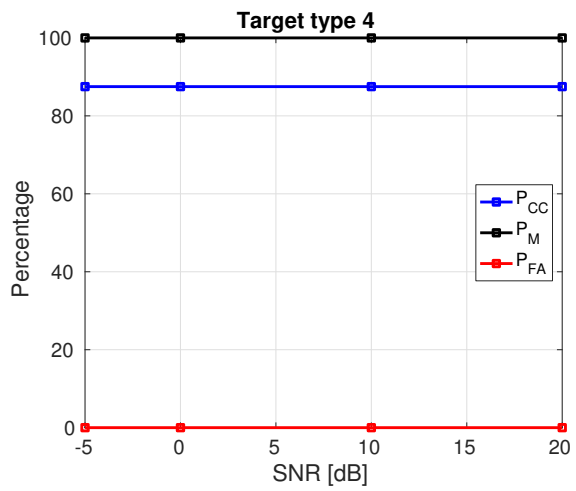


Figure 50: Bayesian, Target 4

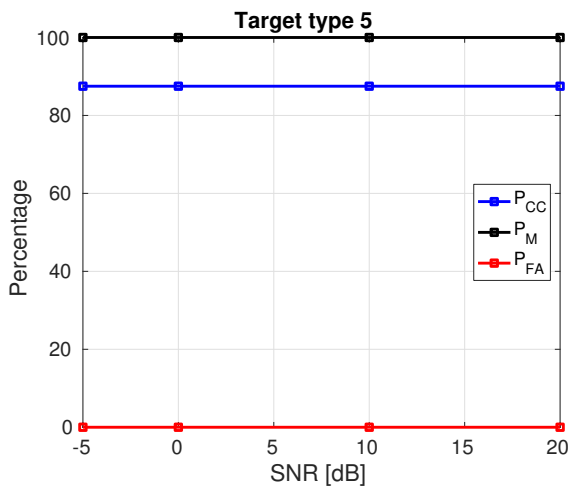


Figure 51: Bayesian, Target 5

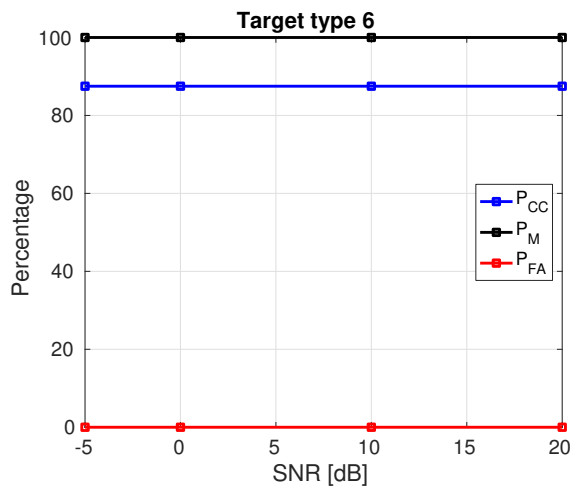


Figure 52: Bayesian, Target 6

LINEAR AND NON-LINEAR TIME-FREQUENCY ANALYSIS  
FOR PARAMETER ESTIMATION OF SPACE OBJECTS

---

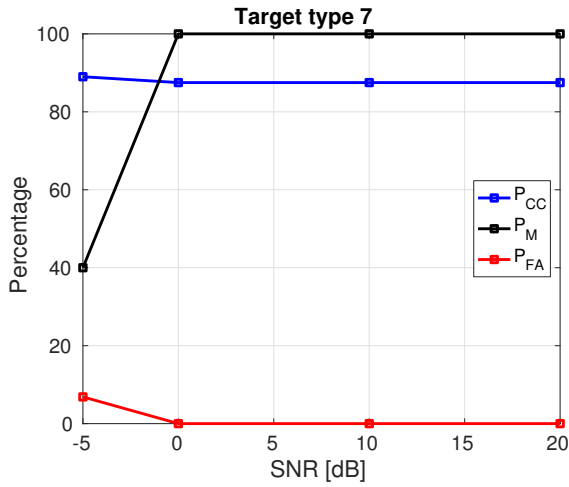


Figure 53: Bayesian, Target 7

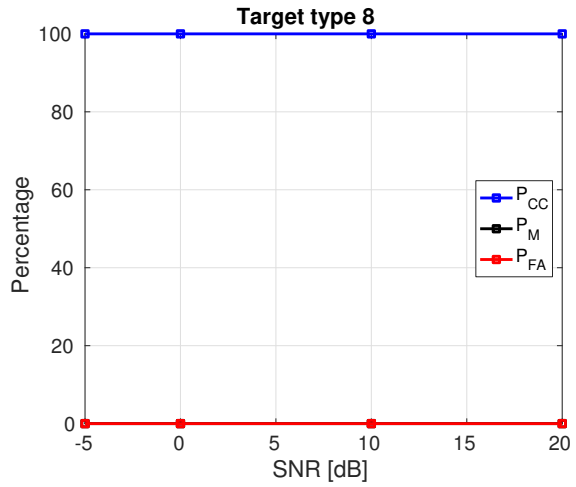


Figure 54: Bayesian, Target 8

The results that we have obtained with the Bayesian classifier are comparable to the ones obtained with the Bayesian classifier using the optical data. Also in this case, the classifier performances are nearly independent of the SNR as the features are quite separable in the feature hyperspace. Only Target 1, Target 2 and Target 8 show good performances. In the other cases, the target is completely missed. The partial conclusion in this case too is that we need to try other classifiers or feature combination.

Figures 55 from 62 show the results for each of the eight target types obtained with the SVM classifier.

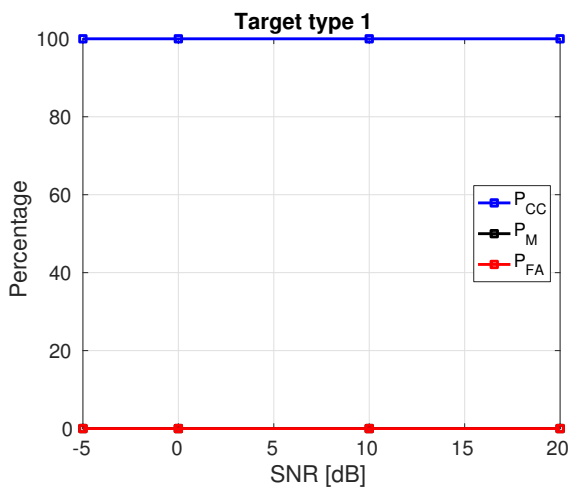


Figure 55: SVM, Target 1

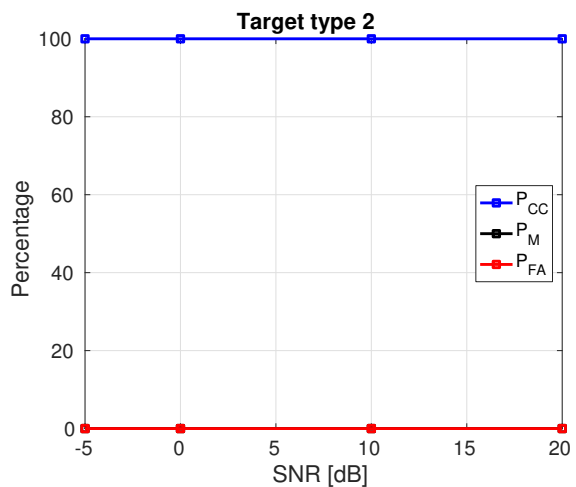


Figure 56: SVM, Target 2

LINEAR AND NON-LINEAR TIME-FREQUENCY ANALYSIS  
FOR PARAMETER ESTIMATION OF SPACE OBJECTS

---

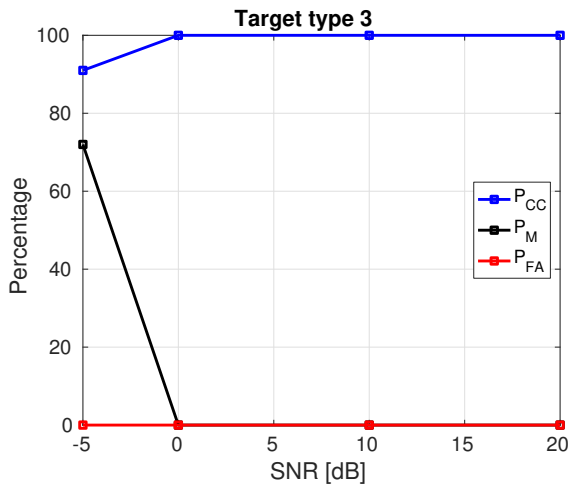


Figure 57: SVM, Target 3

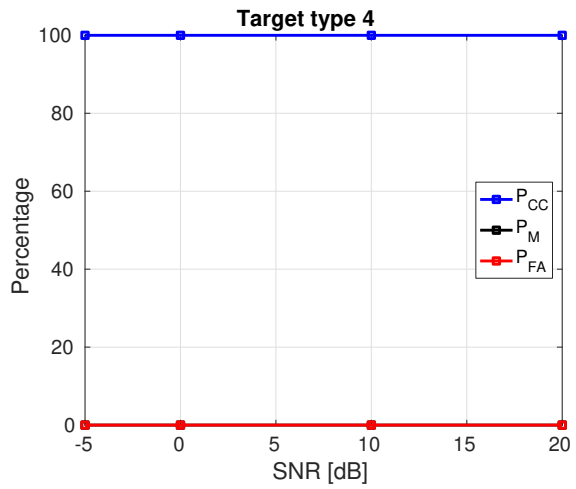


Figure 58: SVM, Target 4

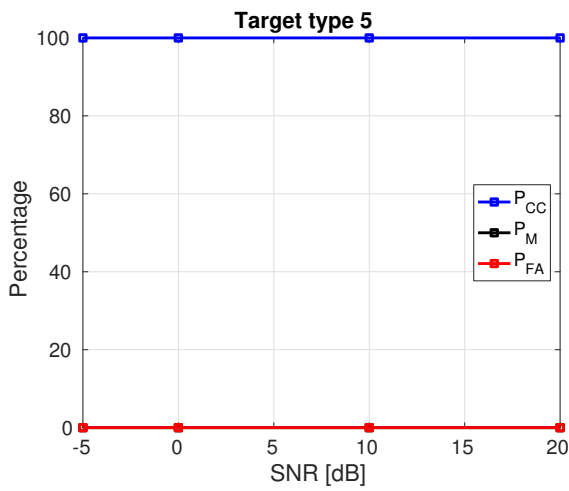


Figure 59: SVM, Target 5

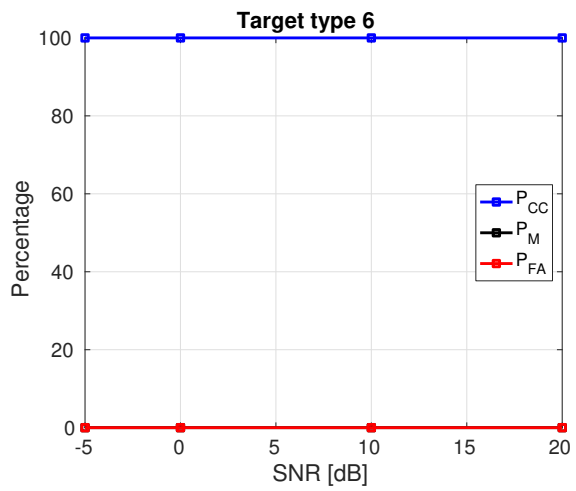


Figure 60: SVM, Target 6

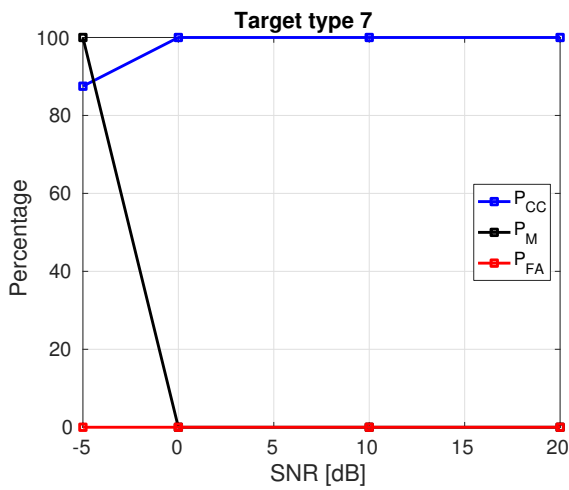


Figure 61: SVM, Target 7

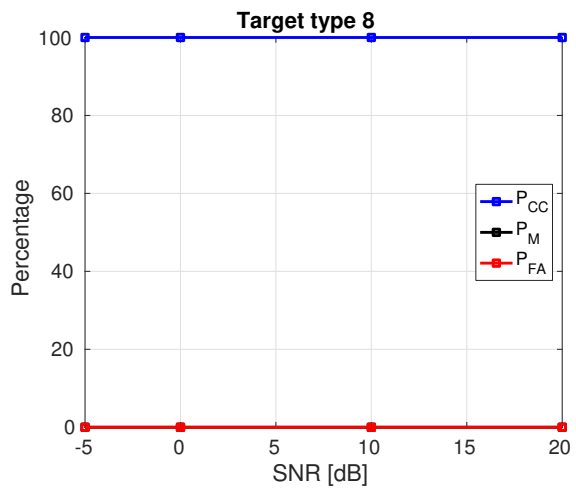


Figure 62: SVM, Target 8

The results that we have obtained using the SVM classifier with radar features show an improvement even when compared against the results obtained in the case of optical features. The various targets are always correctly classified when the SNR is high, and we have only a pair of cases where we have total miss detection at the lowest SNR.

In conclusion, even in this case the simulation results suggest that if we have only radar data, when using the SVM classifier, the results are encouraging.

### 7.3 Fusion

In this section the performance obtained with the fusion of optical and radar features are shown. Even if relatively good results can be obtained by using the SVM classifier, it is interesting to investigate whether the performances can improve further by using a fused feature set, especially when using the Bayesian classifier.

To create the dataset, the simulations were performed by coupling all optical and radar SNRs, therefore obtaining a total of 36 couples. This operation makes sense as two different sensors may not produce the same SNR in their measurements. For each SNR, 25 realizations per class are created. The dataset has 6 features in total, which are the fusion of the selected optical and radar features.

To perform the classifier training, we chose the couple with  $SNR_{OPTICAL} = 45 \text{ dB}$  and  $SNR_{RADAR} = 0 \text{ dB}$ . As already stated this was chosen as an intermediate case and the test was performed also with the same SNR couple.

The following figures represent 3D plots where the blue surface represents the  $P_{CC}$ , the black surface the  $P_M$  and the red surface the  $P_{FA}$ . The two horizontal axes represent the Radar SNR and the Optical SNR, respectively.

Figures 63 from 70 show the results for each of the eight target types obtained with Bayesian classifier.

# LINEAR AND NON-LINEAR TIME-FREQUENCY ANALYSIS

## FOR PARAMETER ESTIMATION OF SPACE OBJECTS

---

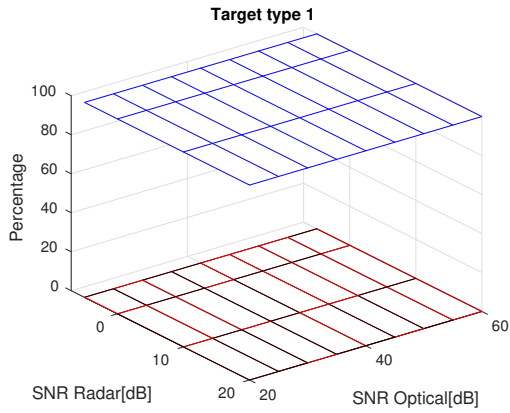


Figure 63: *Bayesian, Target 1*

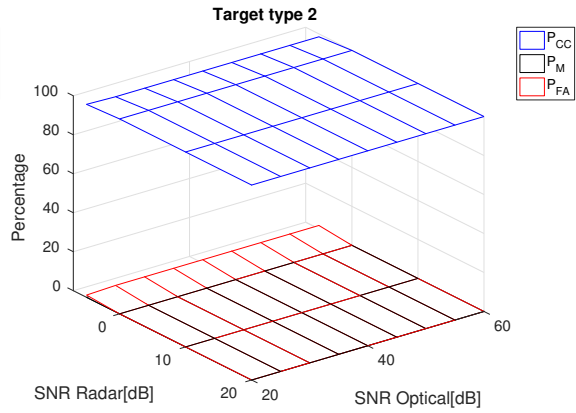


Figure 64: *Bayesian, Target 2*

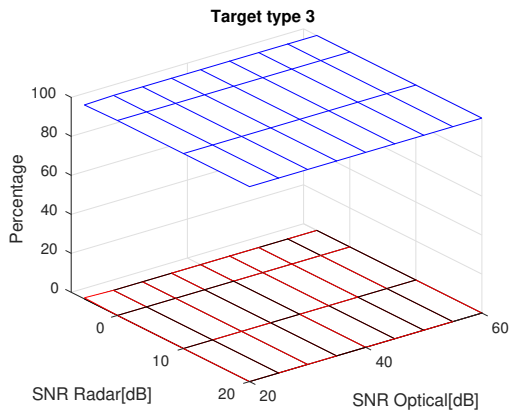


Figure 65: *Bayesian, Target 3*

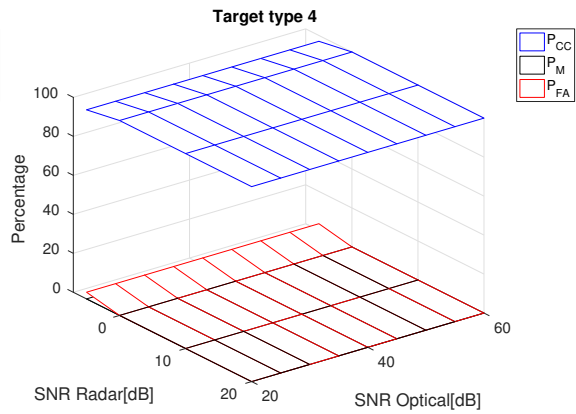


Figure 66: *Bayesian, Target 4*

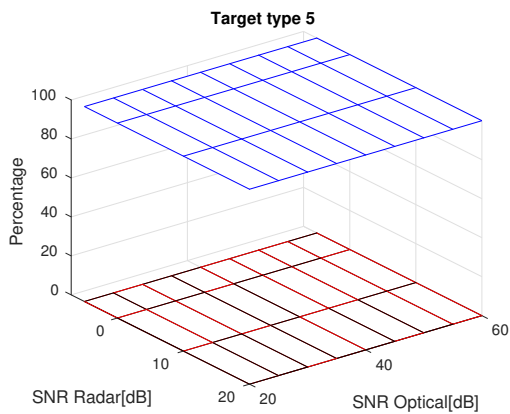


Figure 67: *Bayesian, Target 5*

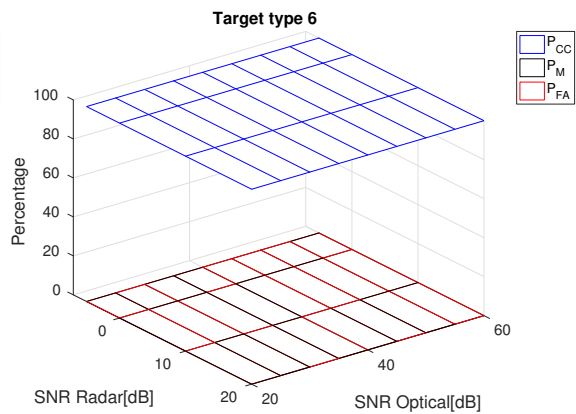


Figure 68: *Bayesian, Target 6*



# LINEAR AND NON-LINEAR TIME-FREQUENCY ANALYSIS

## FOR PARAMETER ESTIMATION OF SPACE OBJECTS

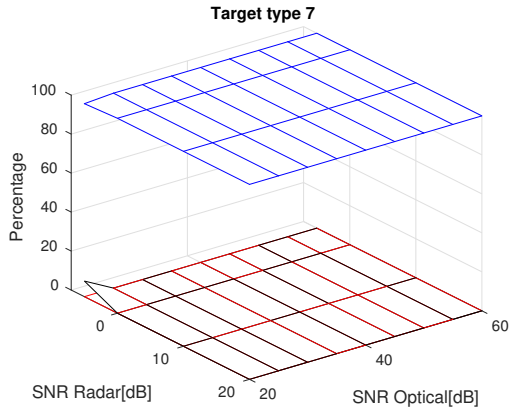


Figure 69: Bayesian, Target 7

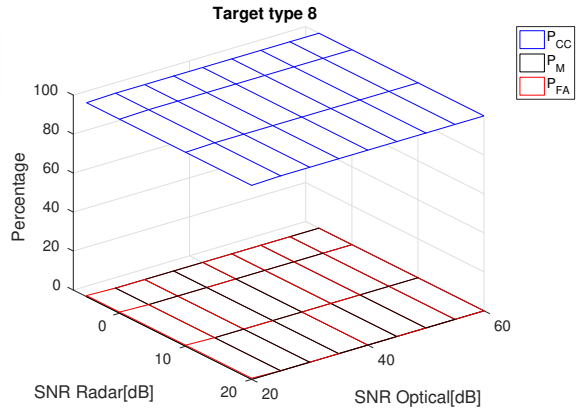


Figure 70: Bayesian, Target 8

It is interesting to note that the Bayesian classifier, when using the fused feature set, performs dramatically better than in the radar-only and optical only cases. The classification performances, in fact, are nearly perfect, save for some small percentage points at the lowest SNR couples. In this case, it is clear that the addition of three more features to each dataset creates a larger (with more dimensions) hyperspace where it is easier to separate the various features, which is then more suited to be utilized with a Bayesian classifier.

Figures 71 from 78 show instead the results for each of the eight target types obtained with the SVM classifier.

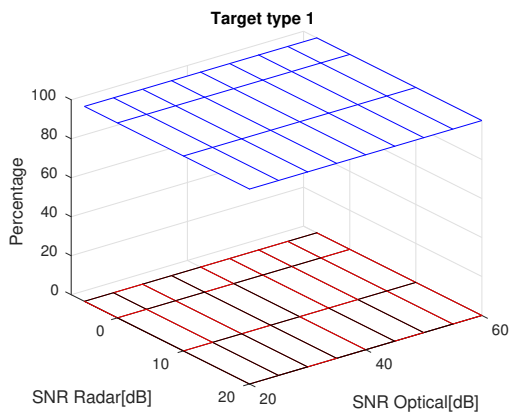


Figure 71: SVM, Target 1



Figure 72: SVM, Target 2

LINEAR AND NON-LINEAR TIME-FREQUENCY ANALYSIS  
FOR PARAMETER ESTIMATION OF SPACE OBJECTS

---

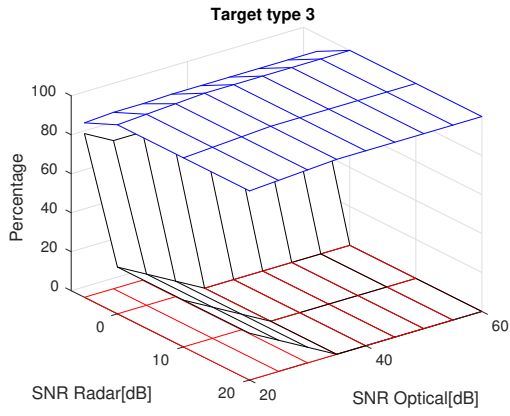


Figure 73: SVM, Target 3

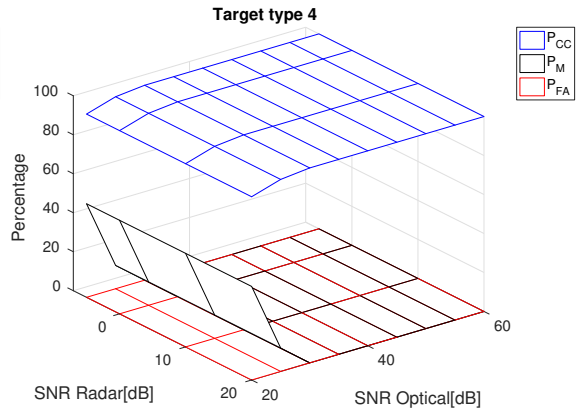


Figure 74: SVM, Target 4

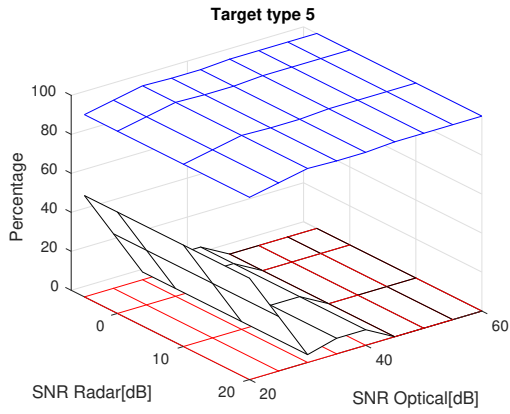


Figure 75: SVM, Target 5

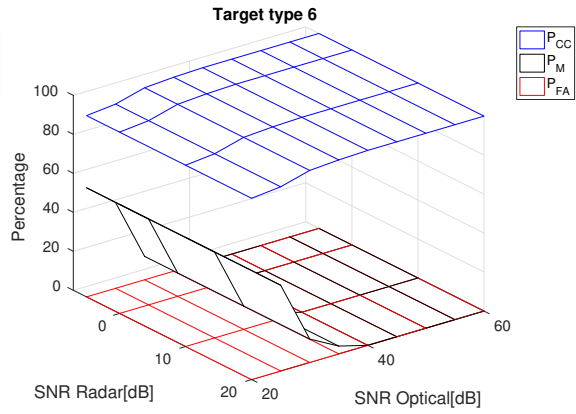


Figure 76: SVM, Target 6

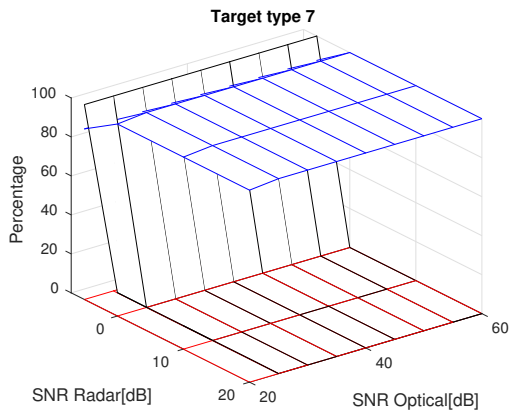


Figure 77: SVM, Target 7

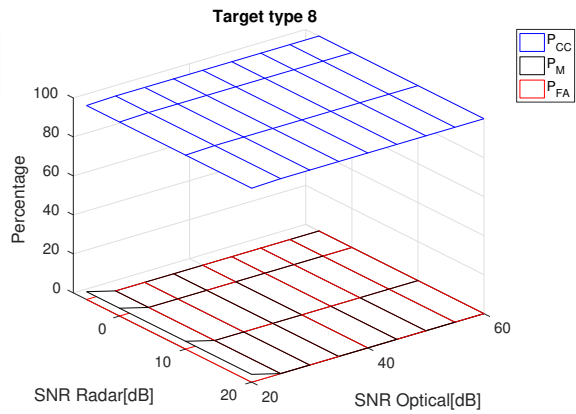


Figure 78: SVM, Target 8

LINEAR AND NON-LINEAR TIME-FREQUENCY ANALYSIS  
FOR PARAMETER ESTIMATION OF SPACE OBJECTS

---

The results obtained with the fusion dataset and SVM classifier are somewhat worse with respect to the results obtained with the Bayesian classifier. By inspecting thoroughly the results, and comparing them to the results obtained in the two previous sections, it is clear that they replicates the SVM results for the two kind of sensors separately. The surfaces from Type 2, 3, 4, 5, 6 have a visible variation only with growing optical SNR and only for  $P_M$ . If we take a 1D section of these surfaces, we obtain the same results for optical sensor data with SVMs. Similarly, Type 3 and 7 for radar data replicates the results obtained with the 1D analysis. It means that the features of fusion 6D hyperplane have the same degree of separability of the 3D hyperplanes generated by optical or radar features only.

In conclusion, while the fusion of features using the SVM classifier does not bring significant advantage (the performances are not degraded), the fusion brings a significant improvement of the performances when using Bayesian classifier.

As a final remark, based on the simulation results, we can say that if we have observations from a single sensor, the SVM classifier has better performances. If data from both radar and optical sensor are available, the Bayesian classifier is the optimal choice. This results must be confirmed with real data before such conclusions can be considered reliable.

## 8 Conclusions

The present technical report has presented some innovative algorithms for estimating RSO parameters. More specifically, by making use of radar data and time-frequency analysis, techniques have been developed that are able to extract and analyse the object's Doppler signature. Some object's physical parameters have been correlated to Doppler signature parameters and estimation techniques have been devised to estimate them. Specifically, the object's rotation speed and the object's size along a specific direction can be estimated to provide additional unique features to be used to discriminate a specific object among others. This concept has been stressed as the techniques and algorithms developed during this project aim to improve data association in tracking and initial orbit determination tasks. The results presented in this technical report show how accurately an object can be discriminated from others when using optical-only, radar-only and joint-optical/radar data. The algorithms have been tested by using simulation data. This may represent a limitation in terms of algorithm validation as the data simulated is not close to realistic scenarios. Nevertheless, as a first step, a controlled simulation environment has allowed for some initial considerations to be made. It is important to note that the results obtained only consider object characteristics that exclude the orbital parameters. The features defined and estimated in this work can be merged with the orbital parameters to define an extended class of tracking algorithms where the data association is aided by the presence of additional information about the object. Some results have highlighted that, without using orbital parameters, in both the cases of optical-only and radar-only measurements, the Bayesian classifier demonstrate that such measurements are insufficient to discriminate objects in a satisfactorily manner. Nevertheless, by jointly using features obtained by processing optical and radar measurements, a high probability of correct discrimination is achieved. The algorithms developed need further validation with real data before a final assessment is made. The members who participated in this project are currently involved in another SST-related project under a government-to-government agreement between Italy and USA. Within such project the problem of data association in RSO tracking with radar measurements will be

LINEAR AND NON-LINEAR TIME-FREQUENCY ANALYSIS  
FOR PARAMETER ESTIMATION OF SPACE OBJECTS

---

carried out by exploiting the algorithms proposed within this project.

## References

- [1] L. Visagie, V. Lappas, S. Erb, “*Drag sails for space debris mitigation*”, *Acta Astronautica*, vol. 109, pp. 65-75, 2015.
- [2] V. C. Chen, “*Time-Frequency Transforms for Radar Imaging and Signal Analysis*”, Artech House, 2002.
- [3] Walker, J.L., “*Range-Doppler Imaging of Rotating Objects*”, in *IEEE Transactions on Aerospace and Electronic Systems*, vol. AES-16, Jan. 1980, p. 23-52.
- [4] Chen, Victor, “*The micro-Doppler effect in radar*”, Artech House, 2011
- [5] M. Dakovic and L. Stankovic, “*Estimation of sinusoidally modulated signal parameters based on the inverse radon transform*”, in *Proc. of the 8th International Symposium on Image and Signal Processing and Analysis (ISPA)*, (2013), p. 302-307.
- [6] L. Stankovic, “*A measure of some time-frequency distributions concentration*”, in *Signal Processing*, Vol.81, No.3, Mar. 2001, pp. 621-631.
- [7] V., Vapnik, “*Estimation of dependences based on empirical data*”, Springer-Verlag, New York, 1982.
- [8] G., Cauwenberghs, and T., Poggio, “*Incremental and decremental support vector machine learning*”, *Adv. Neural Information Processing Systems (NIPS\*2000)*, Cambridge, MA, MIT Press, vol.13, 2001.
- [9] J., Wetson, and C., Watkins, “*Multi-class Support Vector Machines*”, Technical report CSD-TR-98-04, May 1998.
- [10] C.W. Hsu, and C.J. Lin, “*A comparison for multiclass Support Vector Machines*”, *IEEE Trans. on Neural Networks*, vol. 13(2), March 2002.
- [11] T. M. Mitchell, “*Machine Learning*”, McGraw-Hill, 1997

LINEAR AND NON-LINEAR TIME-FREQUENCY ANALYSIS  
FOR PARAMETER ESTIMATION OF SPACE OBJECTS

---

- [12] , Ben K. Bradley, Penina Axelrad, “*Lightcurve Inversion for Shape Estimation of GEO Satellites from Space-Based Sensor*”, ISSFD, 2014
- [13] , Tamara E. Payne, Stephen A. Gregory, Kim Luu, “*SSA Analysis of GEOS Photometric Signature Classifications and Solar Panel. Offsets*”, AMOS Technical Conference Proceedings, 2006
- [14] , Vasiliy S. Yurasov, Vadim G. Vygon, Viktor D. Shargorodskiy, “*Classification and Identification of Geostationary Space Objects by Using Coordinate and Photometric Observations*”, 4th US-Russian - Space Surveillance Workshop, 2000
- [15] , Tamara E. Payne, Keith Lucas, Anil Chaudhary, Shaylah Mutschler, Phan Dao, Jeremy Murray-Krezan, “*A Derivation of the Analytical Relationship between the Projected Albedo-Area Product of a Space Object and its Aggregate Photometric Measurements*”, Proceedings of the Advanced Maui Optical and Space Surveillance Technologies Conference, 2013.